Effect of Vortex Core Stagnation Pressure on Tip Clearance Flow Blockage in Turbomachines

by

Donald L. Cho

Submitted to the Department of Aeronautics and Astronautics
in partial fulfillment of the requirements for the degree of

Master of Science

at the

MASSACHUSETTS INSTITUTE OF TECHNOLOGY

September 1995

Author .....
Department of Aeronautics and Astronautics
August 8, 1995

Certified by .....
Professor Edward M. Greitzer
Professor of Aeronautics and Astronautics
Thesis Supervisor

Certified by .....
Dr. Choon S. Tan
Principal Research Engineer
Thesis Supervisor

Accepted by .....
Professor Harold Y. Wachman
Chairman, Departmental Committee on Graduate Students

Effect of Vortex Core Stagnation Pressure on Tip Clearance Flow Blockage in Turbomachines

by

Donald L. Cho

Submitted to the Department of Aeronautics and Astronautics
on August 8, 1995, in partial fulfillment of the
requirements for the degree of
Master of Science

Abstract

This thesis considers two problems related to turbomachinery tip clearance flows, a generic study of a vortex core in an adverse pressure gradient, and an examination of clearance flow blockage in a transonic rotor for both smooth wall and casing treatment. To address the first issue, an experimental study was carried out to examine vortex core flows in adverse pressure gradients. Data were obtained on core growth as a function of: (i) pressure rise, and (ii) distribution of stagnation pressure in the vortex core. The experimental results were well described by a quasi one-dimensional vortex model. To address the second issue three-dimensional computations were performed of clearance flow blockage in a high speed axial compressor rotor. Casing treatment was modeled as a region of flow injection over the front portion of the blade passage and a region of flow removal from the rear portion. The results showed that the flow injection reduced blockage because of the higher total pressure through the clearance. The suction removed blockage fluid near the endwall from the rear portion of the passage. For the computations investigated it appeared that the suction was the dominant effect.

Thesis Supervisor: Professor Edward M. Greitzer
Title: Professor of Aeronautics and Astronautics

Thesis Supervisor: Dr. Choon S. Tan
Title: Principal Research Engineer

Acknowledgments

I would like to thank my advisors, Professor Edward Greitzer and Dr. Choon Tan, as well as Professor Ian Waitz, for their guidance, advice, and direction over the course of my last two years at the Gas Turbine Laboratory.

Professor Nick Cumpsty and Professor Frank Marble also contributed greatly to this project by meeting with me on their visits. I would like to thank Dr. John Adamczyk from the NASA Lewis Research Center for allowing me to use the code he devloped and for his advice on how to make the proper modifications to that code. I would also like to thank Dr. Mark Celestina from NASA Lewis for his patience in answering my never-ending questions concerning the code.

From around the lab, I would like to recognize Rajesh Khan, Amrit Khalsa, Arif Khalid, Don Hoying, John Brookfield, and Martin Graf for their insights and contributions concerning this project. On a different note, I would like to thank the "Monkey Bunch" and the "Doom Bunch", without whose help this project would never have taken so long. I would also like to acknowledge my office mates and the rest of the Gas Turbine Lab, who include David Underwood, Julian Sell, Willy Ziminsky, Brian Corn, Chris Brown, and Larry Smilg, for keeping me company and providing constant diversion while working on my research.

I would like to thank my parents for their constant support, both financially and emotionally, throughout my years here at M.I.T. And finally, a special thanks to my soon-to-be wife, Jennifer, for her loving support and patience over the last few years.

This work was supported by NASA Lewis Research Center, under Grant #NAG3-1237, Mr. Gary Skoch, Program Manager. This support is gratefully acknowledged.

Contents

List of Figures

List of Tables

Chapter 1

Introduction

Tip clearance vortex flows are of considerable interest in turbomachines. The vortex is the result of fluid leaking through the clearance between the blade tip and the casing. In a compressor, the vortex must pass through a pressure rise, and the resulting growth of the vortex core creates blockage (decreased effective flow area of the blade passage) and hence loss of pressure rise capability.

One method that has been successfully employed to reduce the adverse effects of tip clearance is the use of casing treatment, i.e. slots or grooves cut into the casing over a rotor tip. A proposed mechanism of casing treatment operation involves the injection of high pressure fluid into the core of the clearance vortex; increasing the total pressure in the core results in a decrease in blocked area.

This thesis addresses two fluid dynamic issues relating to this general topic. First, in a basic sense, the tip clearance flow can be described as a vortex core passing through an adverse pressure gradient. To obtain an overall picture of the flow behavior, the behavior of a vortex core is studied in a simple model of this situation. The main aspect addressed, however, is an examination of the clearance flow in a more realistic environment. To this end, a series of numerical experiments are described which focus on the blockage due to tip clearance flow in a transonic rotor.

1.1 Previous Work

There has been much work conducted involving the tip clearance vortices and even more on vortices in general. The following studies were used as the basis for this particular thesis.

The overall behavior of vortex cores in pressure gradients was examined by Brookfield [2] who developed a one-dimensional computational analysis for vortex cores in a confined duct. He also carried out calculations to examine the effect of pressure rise on the tip clearance vortex and on leakage flow behavior.

Khan [11] developed a more general approach to quasi one-dimensional vortex flows in ducts of varying area. The solutions he found had both continuous and discontinuous solutions with rapid core expansion predicted in certain situations. In addition, the flow could be characterized by a non-dimensional swirl parameter which played a role analogous to the Mach number in a compressible flow. Computations were performed to determine the dependence of vortex core growth on non-dimensional parameters corresponding to the core axial velocity, the core area, and the swiwl. The model showed good agreement when compared with results from a Navier-Stokes solver and with experimental data.

Tip clearance flows were analyzed by Smith [17] in a landmark paper. He related the axial velocity boundary layer displacement thickness, tangential force deficit thickness, static pressure rise, and efficiency using data from a number of low speed compressors. He related a normalized displacement thickness to the ratio of stage pressure rise to maximum stage pressure rise, and to the tip clearance normalized by the staggered spacing. This work illustrated the importance of the casing boundary layer, and the clearance related blockage, in setting the pressure rise.

Khalid [9] used three-dimensional Navier-Stokes calculations to study the influence of the tip clearance flow on the compressor pressure rise. The calculations showed that the clearance flow, which leads to low total pressure fluid in the core of the vortex, is a major factor in blade passage blockage. Khalid also found a parametric dependence between this blockage and the static and total pressure changes experienced by the

core. The computational data was also shown to correlate well with a simple two-dimensional wake model proposed by Hill et al.[7].

There have also been a number of studies of casing treatment. Those having the most relevance to the present work are described below. Takata and Tsukuda [19] performed experiments on casing treatment in low speed axial flow compressors. Data was taken on overall compressor performance and on flow through the blade row. Data was also taken on the flow within the slots of the casing treatment. Based on these results, Takata and Tsukuda suggested momentum exchange between the jet emerging from the treatment and the main flow as a possible mechanism for the stall margin improvement for compressors with casing treatment.

Smith and Cumpsty [16] experimented with axial skewed slot casing treatment on a low speed compressor rotor. Measurements of the loss downstream of the rotor were taken, as well as data on the flow in the blade passage and within the treatment slots. It was tentatively determined that the unsteady effects associated with the slot flow are of secondary importance. Smith and Cumpsty concluded that removal of high swirl, high loss fluid from the endwall near the trailing edge of the pressure surface and injection of this fluid with the direction of absolute swirl reversed near the leading edge of the blade was of primary importance.

Crook [3] used a three-dimensional Reynolds-averaged Navier-Stokes calculations to explore the effects of casing treatment on a compressor stator. The core of the clearnace vortex was found to contain high loss fluid which was identified as a source of blockage. The calculations showed that the casing treatment contributed to the reduction of blockage by removing low total pressure fluid at the rear of the passage and by energizing the flow in the tip clearance vortex core, but did not attempt to quantify the two processes.

1.2 Objectives

The objectives of this thesis are two fold and are both related to the behavior of the tip clearance vortex. First, a set of experiments were conducted to obtain data on

the behavior of vortices in a pressure gradient with different core stagnation pressure distributions. The purpose is to gain understanding of the general problem of the effect of core stagnation pressure on vortices in pressure gradients, which is one aspect of the casing treatment injection process.

The primary objective, however, was to obtain information on casing treatment operation in high speed compressors using a three-dimensional Navier-Stokes solver. Flow situations with and without casing treatment were examined to assess the effect of casing treatment on tip clearance related blockage. The endwall flow and the clearance flow were studied in detail to see how casing treatment affected these areas. The goal was to isolate those effects associated with the casing treatment flow that are the main mechanisms for blockage reduction.

1.3 Contributions

The contributions of the work presented in this thesis are as follows:

- A simple experiment was performed to demonstrate the effect of core stagnation pressure on vortices passing through a pressure gradient. A quasi one-dimensional model was found to describe the resulting behavior well..

- Blockage data obtained using a three-dimensional Navier-Stokes flow solver is presented for a supersonic rotor with and without casing treatment. The effects of casing treatment flow on compressor blockage were investigated, and the blockage reduction quantified. The links between injection and suction and blockage were also addressed. Flow injection from the casing treatment was found to reduce blockage by directly affecting the clearance flow stagnation pressure. Suction in the rear of the blade passage into the casing treatment removed blockage fluid near the endwall.

1.4 Organization of the Thesis

Chapter 2 describes an experiment designed to examine the behavior of a vortex passing through pressure gradients of varying magnitudes. Chapter 3 discusses the results of the experiment and compares them to a one-dimensional vortex model. Chapter 4 discusses blockage calculations analogous to those of Khalid [9] in a high speed rotor with a smooth casing. Chapter 5 then explores the effects of casing treatment on the tip clearance vortex using a model of the casing treatment similar to that of Crook [3]. Chapter 6 presents the summary and conclusions.

Chapter 2

Experimental Setup and Data Acquisition

2.1 Experimental Design

An experiment was designed to study the effect of core stagnation pressure level on a vortex in an adverse pressure gradient; specifically, how core total pressure affects vortex core growth. This aspect of the experiment has links to the effect of casing treatment on tip clearance flows. The experiment was designed to be an abstraction to the generic situation of Khalid[9] and Khalsa[10] who used geometries and flow fields which more closely resembled the actual compressor flow. One question, therefore, was how closely the two situations correspond.

At the most basic level the experiment consists of creating a vortex core and passing it through a pressure gradient. The facility, however, had to be designed so flow parameters could be controlled to study their effect. Specifically, we needed the capability to vary swirl, core total pressure, and static pressure rise over regimes that are of interest for modern axial compressors.

2.2 Experimental Facility

An experimental facility with the ability to control the desired parameters was built by Hardie and Lengyel[6] who also conducted the initial tests. Figure 2-1 shows the test rig. It consists of a seven foot long, seven inch inner diameter, clear plexiglass tube with a bell mouth inlet open to the atmosphere and the other end connected to a blower by flexible hose. A removable plate with inlet guide vanes is placed against the bell mouth, creating a channel (two and a half inches wide) for the the flow to enter the rig. The flow passes through the guide vanes and into the plexiglass tube. By adjusting the angle of the vanes, the initial swirl can be controlled.

Roughly twenty inches from the bell mouth, six flow extraction sections are located. These create the pressure gradient in the tube. Each section consists of a square plenum surrounding the plexiglass tube. Flow is drawn into the plenum through a set of slits in the tube. Each section is connected through a ball valve into a large manifold which is connected to the blower. By adjusting the ball valves between the chambers and the manifold, different levels of pressure rise can be achieved. Figure 2-1 shows the location of these pressure chambers on the main tube.

Figure 2-2 shows the flow extraction section/manifold setup. The main tube and the manifold tube are connected to the blower through a three way valve with the third valve opening acting as a bleed (from atmosphere). Adjusting the valve settings controls the velocity in the tube and the magnitude of the pressure gradient.

Fluid was injected into the vortex core through a small hole down the center of the cone on the vane plate. The injection is from a high pressure, compressed air source and the level of core injection was controlled by a valve upstream of the cone.

2.3 Data Acquisition

Data acquisition involved use of a three-hole wedge probe and a Kiel probe. The three-hole probe was calibrated to give measurements of the flow angle and the dynamic pressure. The wedge probe was originally intended to measure total pressure as well,

but initial tests showed that the error could be greater than ten percent for flow angles greater than ten degrees and thus was unacceptable. The Kiel probe was therefore used to obtain the total pressure.

Measurements were taken at an upstream station four inches in front of the first flow extraction section, and at a downstream station four inches behind the last flow extraction section. These are indicated as U (upstream) and D (downstream) in Figure 2-1. The wall static pressure was also measured at the two locations.

At each station, the pressure readings were taken at 47 points along the diameter of the tube with the probe moved between points by a motorized traverse. A set of pressure transducers was used to convert the pressure readings to voltages, which were then processed by the computer used to coordinate the data acquisition process.

2.4 Test Matrix

Tests were conducted varying vane angle, pressure gradient, and core injection. The inlet velocity was kept constant for all test conditions. The maximum dynamic pressure (about 550 to 600 Pa) was limited by the integrity of the flexible hose used to connect the blower to the test rig. Conditions were maintained near this maximum value to keep the resolution as high as possible.

Characteristics of a typical tip clearance vortex were given by Khalid[9] and Khalsa[10]. They determined that representative maximum swirl levels are roughly 25 degrees, pressure rise is 40 to 60 percent of the inlet dynamic head, and core total pressure defect at the initiation of the pressure rise is 50 percent of the inlet dynamic head. The test conditions were based on these values.

Three different vane angles were selected: 5, 10, and 15 degrees, resulting in maximum swirl angles of about 15, 25, and 35 degrees at the upstream location. The middle swirl level was chosen to correspond to the maximum swirl level of the typical tip clearance vortex. The other two swirl levels were chosen as low and high swirl cases to bracket this case.

Tests were conducted at three levels of pressure rise as well: 0, 50, and 75 percent

of the inlet dynamic head. Again, the middle level was meant to correspond to the pressure rise experienced by a "typical" tip clearance vortex at a high loading condition. The high pressure rise was the maximum achievable, again due to constraints related to the flexible hoses.

Originally, three core injection levels were to be tested, corresponding to a total pressure defect in the core, no defect, and a total pressure excess in the core. However, as the level of swirl and the level of core injection were changed, the size of the vortex core changed. According to Khalid and Khalsa, the initial width of the clearance vortex core is related to the clearance height. Changing the vortex core width between different test conditions would then make it difficult to directly compare data since it would be analagous to changing the compressor clearance height. It was thus desirable to maintain constant initial core width. Only in the low swirl cases could the total pressure defect, constant, and excess be achieved with this restriction. In the moderate swirl case, the total pressure excess case could not be achieved, and a moderate total pressure defect case was run instead. In the high swirl case, the constant total pressure case could not be achieved without changing the initial core size. As a result, only a no injection and a high injection case was tested which gave a high and moderate total pressure defect. The resulting total pressure defects for all cases are shown in Table 2.1.

A total of 24 test cases were performed. Data traverses with both the wedge probe and the kiel probe were taken at the upstream and downstream location, a total of four traverses, for each testing condition. The resulting data were swirl angle, dynamic head, and total pressure profiles at the upstream and downstream locations. The test matrix is outlined in Table 2.1.

Samples of the data from these traverses can be found in Appendix A.

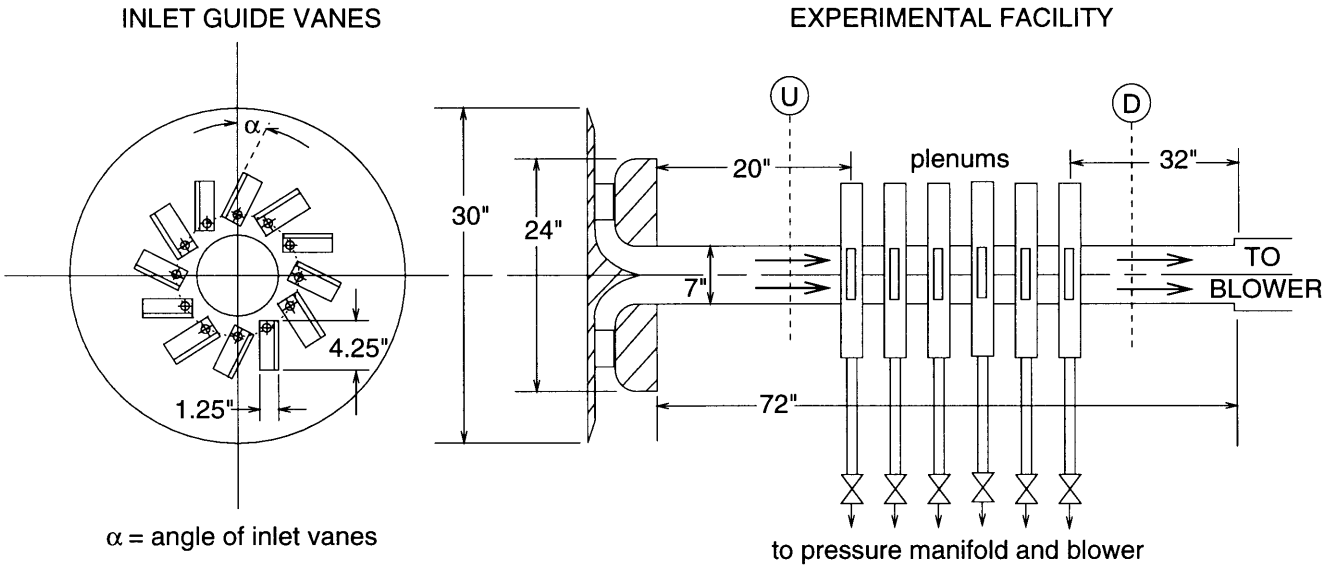

Figure 2-1: Schematic of Experimental Facility

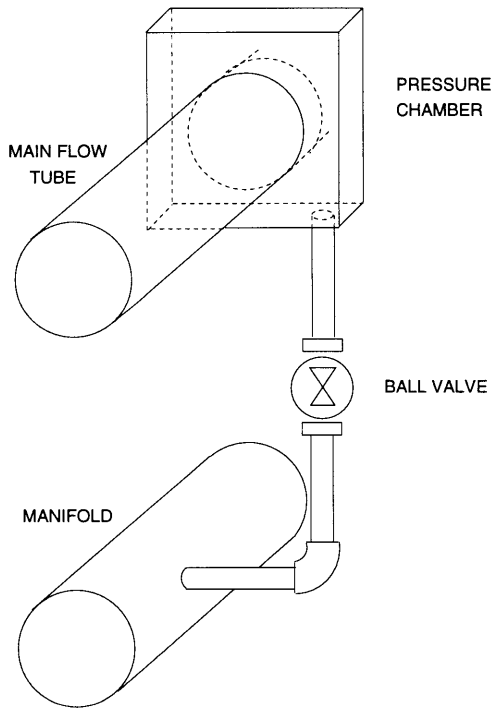

Figure 2-2: Pressure Chamber and Manifold Setup

Vane Angle (degrees)	Max Swirl Angle (degrees)	Static Pressure Rise (percent inlet Q)	Core Injection (psi)	Core P_t Defect ($\frac{\Delta P_t}{Q}$)
5	15	0	0	-0.5
			20	0.0
			35	+0.4
		50	0	-0.5
			20	0.0
			35	+0.4
		75	0	-0.5
			20	0.0
			35	+0.4
10	25	0	0	-0.5
			25	-0.3
			35	0.0
		50	0	-0.5
			25	-0.3
			35	0.0
		75	0	-0.5
			25	-0.3
			35	0.0
15	35	0	0	-2.4
			40	-0.6
		50	0	-2.4
			40	-0.6
		75	0	-2.4
			40	-0.6

Table 2.1: Outline of Test Conditions

Chapter 3

Experimental Results

3.1 One-Dimensional Vortex Model

Before reviewing the results, it is useful to briefly describe the one-dimensional vortex model which we used for understanding the experiments. It is not the purpose here to review the work. Two recent views of the problem have been by Darmofal [5] and Brookfield [2] who used a quasi one-dimensional model for the behavior of vortex flows in pressure gradients. The model was based on a control volume approach similar to that of Landahl and Widnall [13]. The model predicts many features of vortex flows despite its simplicity.

An extension of this model for confined flow has been developed by Khan [11] using the description set up by Brookfield [2]. The flow is taken as incompressible and axisymmetric. There are two regions: a vortex core flow and an outer flow. The flow in the core is assumed to contain all the axial vorticity, and the outer flow is taken as irrotational. The pressure distribution is given by simple radial equilibrium.

The swirl velocity distribution in the core is given by a Rankine distribution, swirl velocity proportional to radius. The outer flow has swirl velocity inversely proportional to the radius. The axial velocities are uniform in the core and in the outer flow. So that there can be a possible discontinuity in the axial velocity profile at the core edge. The flow model is outlined in Figure 3-1.

With the above assumptions, conservation of mass and momentum in their integral

forms were used to derive the model equations. Khan solved these equations to give the overall parametric behavior [11]. The relevant nondimesional parameters affecting core growth ratio, δ (the ratio of exit to inlet core radius), were found to be inlet swirl ratio, Ω_0, and static pressure rise normalized by the core dynamic head, $\frac{\Delta p}{Q_c}$. The ratio of the exit core radius to inlet core radius can thus be expressed in terms of the inlet swirl ratio and the normalized static pressure rise. These solutions are compared to the experimental results below.

3.2 Comparison of Experimental Data to Vortex Model

The changes in core centerline static pressure and in core edge static pressure were used as alternative measures of pressure rise. These are independent of how the pressure rise was achieved, i.e. by varying duct area or by suction. Vortex core growth can be expressed either in terms of the rise in core centerline static pressure or in terms of the rise in core edge static pressure.

One difference between experiment and model was the axial velocity in the the core. As in Figure 3-2, the experimental velocity profile was continuous, but that in the model was not. In the comparisons, an averaged core dynamic head was used as the value for Q_c to normalize the pressure changes. Two types of averaging were used, area and defect averaging; the first for simplicity, and the second because the magnitude of the velocity defect in the vortex core plays a major role in vortex behavior. The defect averaging weights the average according to the magnitude of the defect in axial velocity at each point in the core. These will be commented upon subsequently.

In terms of centerline pressure, Khan showed that the following relationship holds:

$$\frac{\Delta p_c}{Q_c} = 1 + \Omega_0^2 - \frac{\Omega_0^2}{\delta^2} - \frac{1}{\delta^4} \tag{3.1}$$

where Δp_c is the change in centerline static pressure

Equation 3.1 shows that the core radius ratio depends on the initial level of swirl as well as the change in centerline pressure.

The experimental data are compared to the model in Figures 3-3, 3-4, and 3-5 which show core radius ratio versus normalized centerline static pressure rise. Figure 3-3 compares the model and the experimental results, using area averaging, for the low swirl level (vane angle = 5 degrees) and the three core injection levels. The core injection levels are indicated in the legend. Although the swirl varied slightly with the different injection levels, the three cases were put on the plot using an average swirl level since the variation in swirl produced only a small change in the theoretical curve. Figures 3-4 and 3-5 show similar comparisons for the medium and high swirl levels, respectively.

The plots for the low and medium swirl levels show good agreement between the experimental data and Khan's simple model. For the high swirl level plot, the case with 40 psi core injection agrees well with the theory, but the case without core injection shows poor agreement. For this case, the axial velocity defect in the core is large, and the normalized pressure rise is very high. Darmofal [5] has calculated the point at which vortices will begin to experience large core growth in response to a pressure gradient. The critical normalized pressure rise, $\frac{\Delta p_c}{Q_c}|_{crit}$, for a given initial swirl level is given by:

$$\frac{\Delta p_c}{Q_c}|_{crit} = 1 + \Omega_0^2 - \frac{3\Omega_0^4}{4} \tag{3.2}$$

For pressure rises greater than the critical values, the theoretical model may be less accurate as a description of the actual flow because when the vortex is experiencing rapid core growth, the assumption that the radial velocity component is negligible is no longer valid. Using equation 3.2, the critical pressure rise can be calculated. For the high swirl case, the critical normalized pressure change is about 1.24, and it can be seen the pressure rises are greater than this critical value for the data that does not agree with the model. For information regarding the behavior of vortices in this regime, refer to Darmofal[5] and Khan [11].

Figures 3-6, 3-7, and 3-8 show the comparison between the same experimental and

the theoretical data compared above, except that defect averaging has been used to calculate the average core dynamic head instead of area averaging. The two sets of plots are similar, although the area average gives slightly better agreement between experiment and model.

In terms of the core edge static pressure, the core growth is given by:

$$\frac{\Delta p_e}{Q_c} = 1 - \frac{1}{\delta^4} \tag{3.3}$$

where Δp_e is the change in core edge static pressure, and Q_c is the core axial dynamic pressure. The explicit dependence on the initial swirl ratio has dropped out (although the presence of swirl is still a major factor). The relation between core radius ratio and normalized edge pressure thus collapses to one curve.

Using core edge static pressure, the experimental and analytical data can be compared on a single plot, as shown in Figures 3-9 and 3-10, using area averaging and defect averaging, respectively. Both plots show good agreement between the experimental and theoretical data for low pressure rises, i.e. the region where the vortex core experiences small core growth for a given pressure rise. Where the core experiences rapid core growth, the experiment and the theory do show similar trends, but there is a difference in the region of large core expansion. This issue is addressed in the next section.

3.3 Dependence on Axial Velocity Profile

From Figure 3-9 and Figure 3-10, one can see that the experiment and the analysis show similar trends, but that the theory overpredicts the point of criticality (rapid core growth). A potential source of this discrepancy is the difference between the experimental and theoretical axial velocity profiles. Khan used a top-hat velocity profile in his model, while the experimental case showed a continuous velocity profile.

To see whether this difference would account for the discrepancy between the experiment and theory, the calculations were redone (in a joint effort with Khan) using

a velocity profile that more closely resembled the experimental case. A wake profile used by Hill et al. [7] was used as the velocity distribution for the new calculations. The profile was given by the equation:

$$\frac{U-u}{U} = \beta[1 - (\frac{y}{b})^{\frac{3}{2}}]^2 \tag{3.4}$$

where

U = freestream axial velocity

u = core axial velocity at a given radius

$\beta = \frac{U-u_c}{U}$

u_c = centerline axial velocity

b = core radius

For β less than one, the velocity profile has a velocity defect in the core and for β greater than one the profile has an excess in the core. The Hill wake profile is shown in Figure 3-11.

Calculations were performed to predict the vortex core growth as a function of the core edge pressure rise. These results were then compared to the results for the top-hat velocity profile cases using area averaging and defect averaging. The results for a velocity defect in the core is shown in Figure 3-12. The curve for the Hill profile was stopped at the point where reverse flow appeared at the centerline of the core. The effect is to shift the vortex core growth curve to the left, i.e. rapid core growth occurs at a lower normalized pressure rise, closer to the data. The additional total pressure defect on the centerline which is not accounted for when the velocity is averaged causes the rapid rise in core growth to occur at a lower core edge pressure rise.

The velocity excess case, shown in Figure 3-13, shows the opposite effect, as would be expected. The core growth curve is shifted to the right. So for the velocity excess cases, using a continuous profile actually shifts the core growth curve away from the data. Using a continuous axial velocity profile thus would not account for the discrepancy between the experimental data and the theoretical data. While other

explanations can be given (e.g. differences in turbulent mixing), the basic idea here is to understand the parametric trends rather than develop a detailed analysis; hence, this avenue was not pursued further.

3.4 Comparison to Tip Clearance Vortex

Comparing the experiment to tip clearance data has met with less success than comparing directly to the model. An attempt was made to correlate the vortex data to tip clearance data in terms of various blockage and loading parameters. The details of these parameters are discussed in the following chapter and in Khalid [9]. Plotting the blockage parameter versus the loading parameter is conceptually similar to plotting vortex core size versus pressure rise, as was performed earlier. However, plotting the data in terms of these parameters did not give agreement with Khalid's data. One of the objectives of the experiment was to find a link between the general vortex parameters (i.e. core size and pressure rise) and tip clearance flow parameters (i.e. blockage and loading). This link has yet to be established.

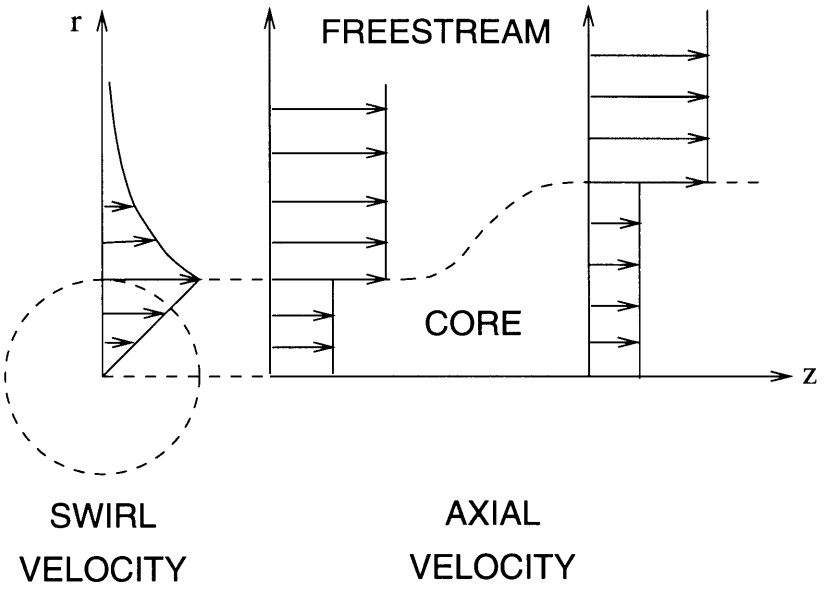

Figure 3-1: Structure of Flow Modeled by Khan

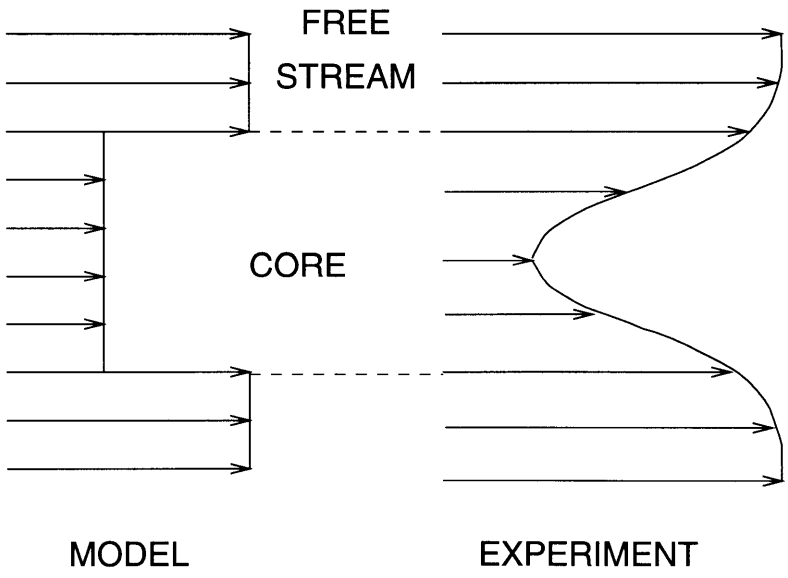

Figure 3-2: Axial Velocity Profiles: Model and Experiment

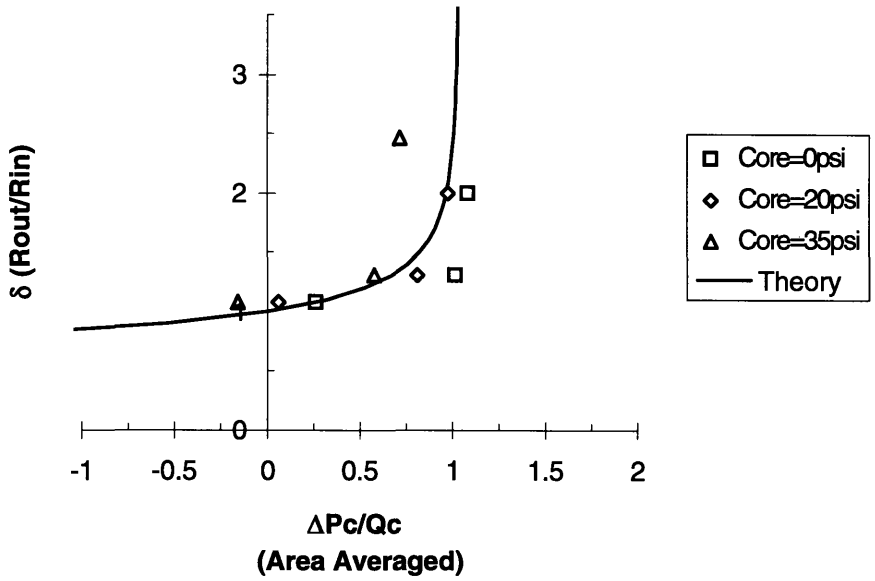

Figure 3-3: Comparison of Experimental and Theoretical Data in Terms of Normalized Centerline Pressure Using Area Averaging for Vane Angle=5 and for Three Core Injection Levels

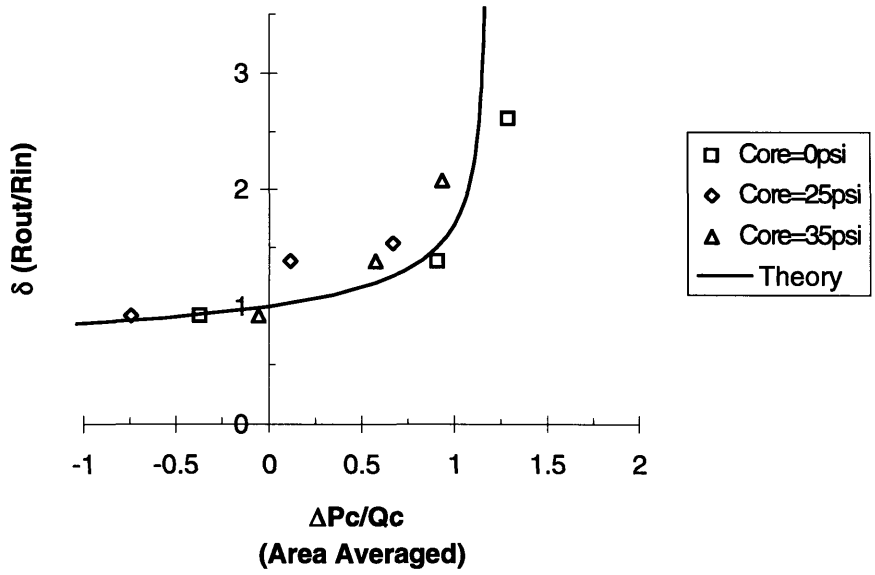

Figure 3-4: Comparison of Experimental and Theoretical Data in Terms of Normalized Centerline Pressure Using Area Averaging for Vane Angle=10 and for Three Core Injection Levels

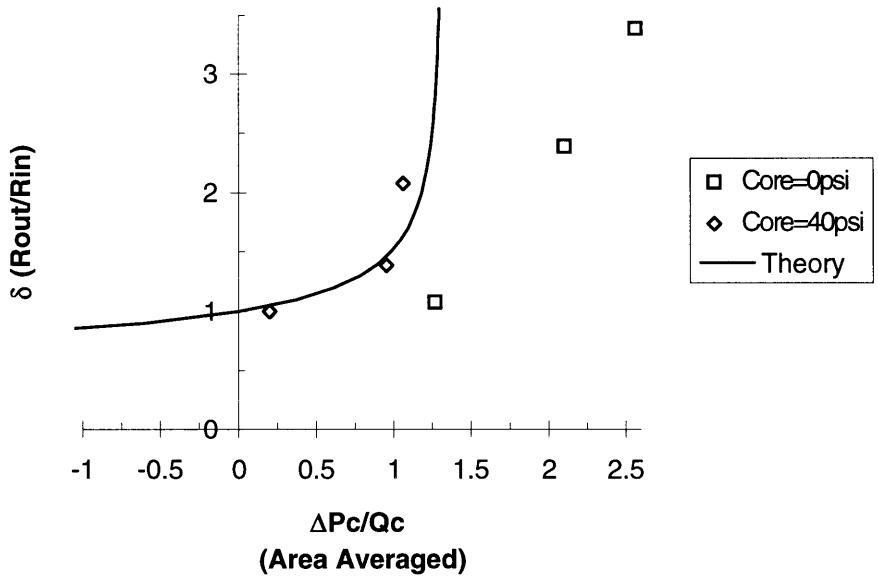

Figure 3-5: Comparison of Experimental and Theoretical Data in Terms of Normalized Centerline Pressure Using Area Averaging for Vane Angle=15 and for Two Core Injection Levels

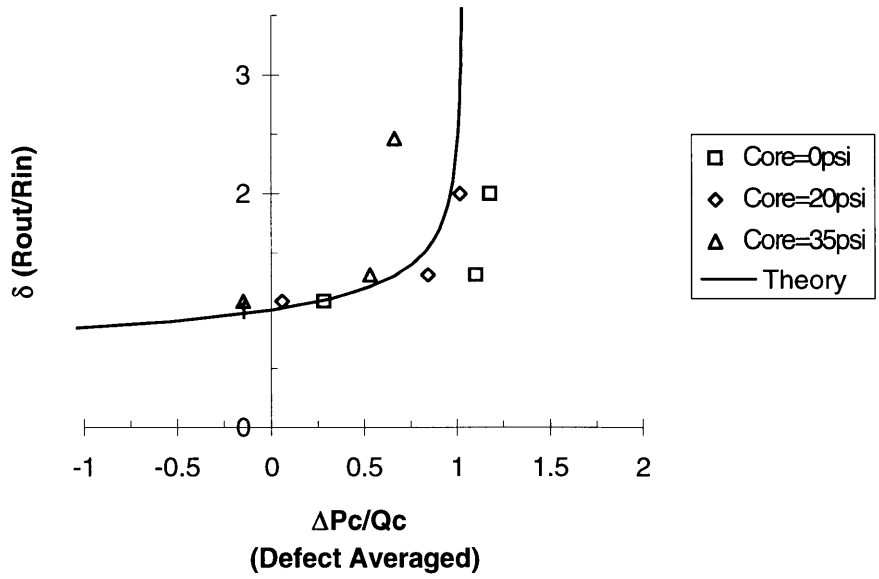

Figure 3-6: Comparison of Experimental and Theoretical Data in Terms of Normalized Centerline Pressure Using Defect Averaging for Vane Angle=5 and for Three Core Injection Levels

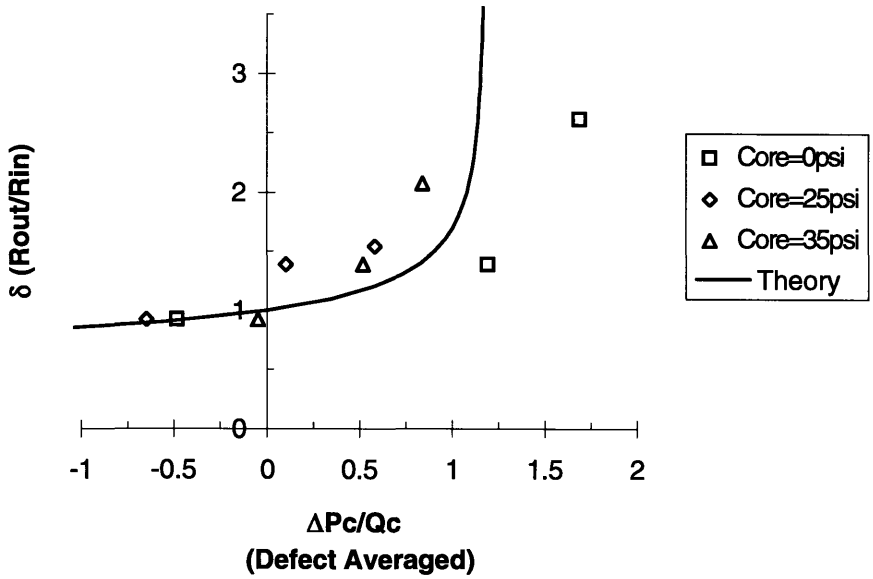

Figure 3-7: Comparison of Experimental and Theoretical Data in Terms of Normalized Centerline Pressure Using Defect Averaging for Vane Angle=10 and for Three Core Injection Levels

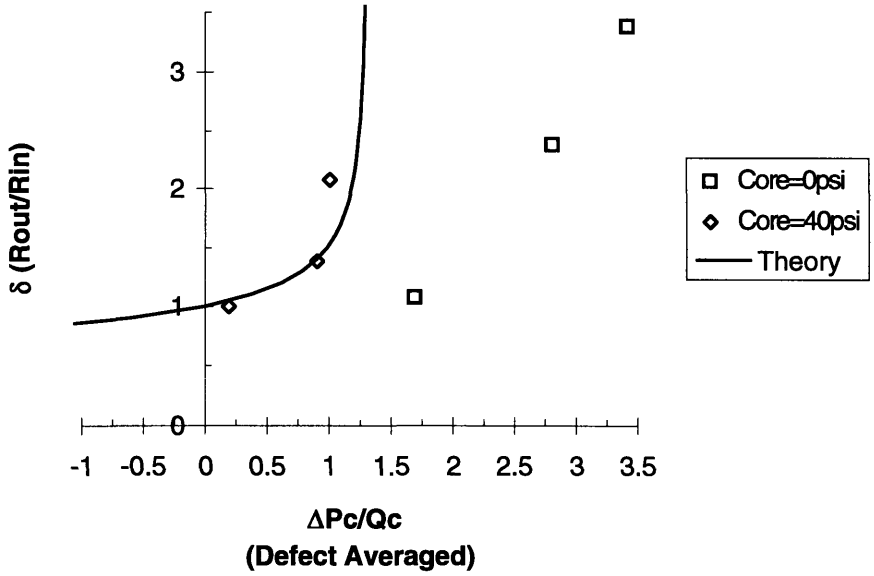

Figure 3-8: Comparison of Experimental and Theoretical Data in Terms of Normalized Centerline Pressure Using Defect Averaging for Vane Angle=15 and for Two Core Injection Levels

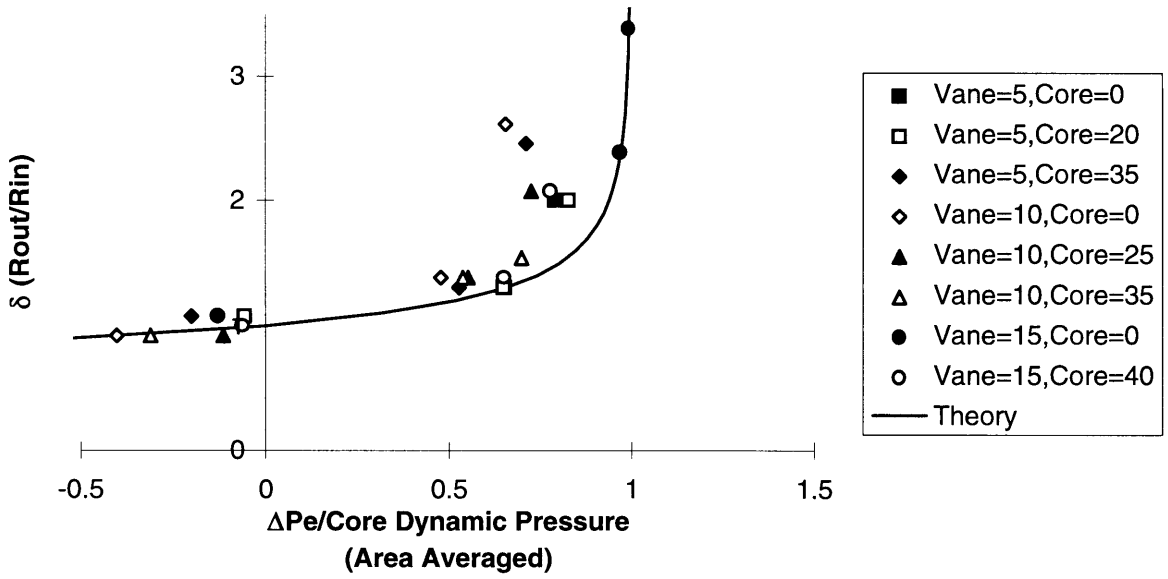

Figure 3-9: Comparison of Experimental and Theoretical Data in Terms of Normalized Core Edge Pressure Using Area Averaging

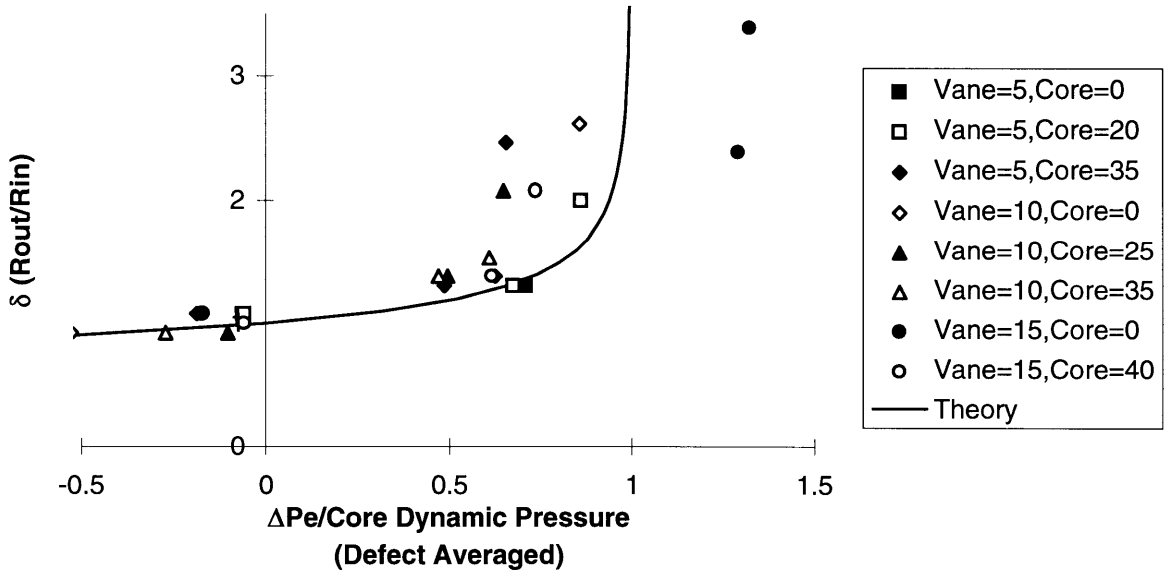

Figure 3-10: Comparison of Experimental and Theoretical Data in Terms of Normalized Core Edge Pressure Using Defect Averaging

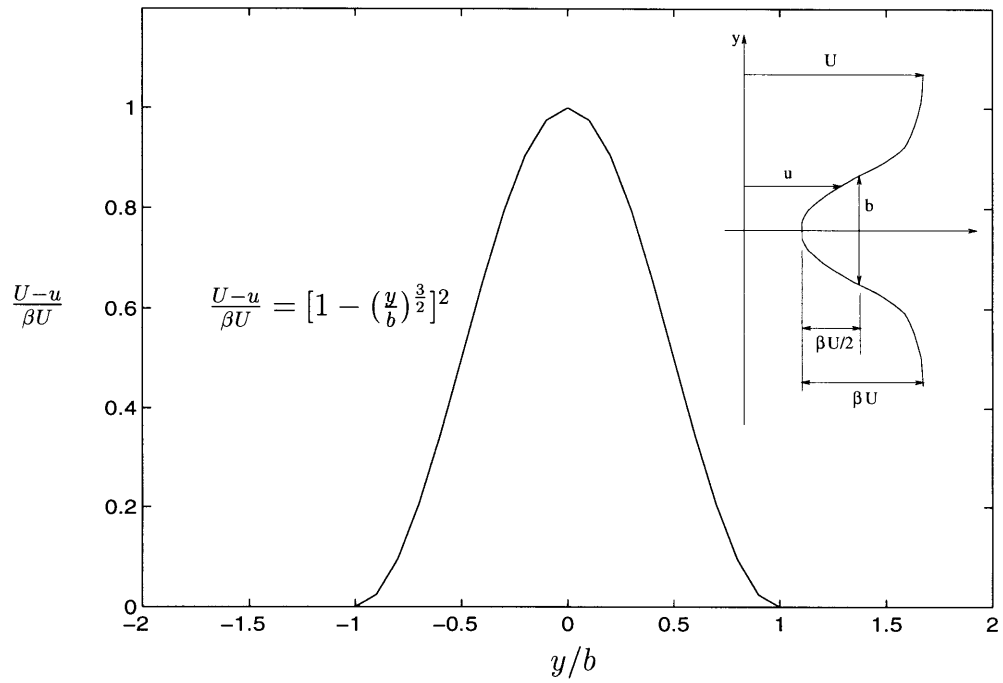

Figure 3-11: The Hill Wake Profile

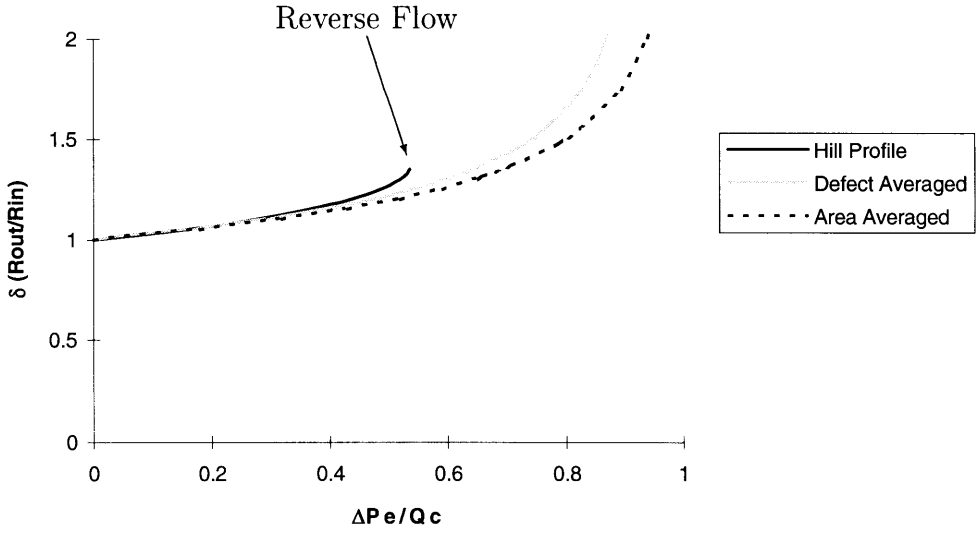

Figure 3-12: Comparison of Vortex Core Growth for Top-Hat and Continuous Velocity Profile Vortices with a Velocity Defect in the Core

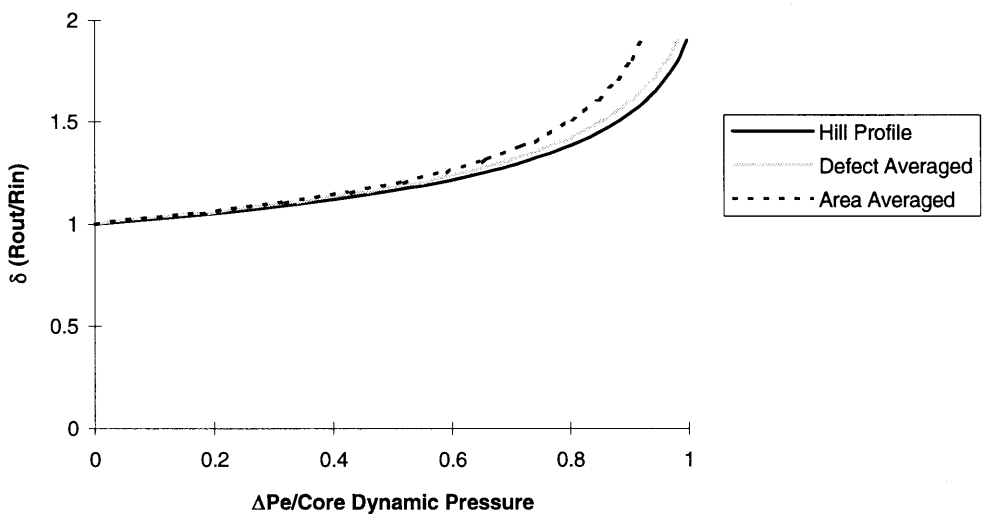

Figure 3-13: Comparison of Vortex Core Growth for Top-Hat and Continuous Velocity Profile Vortices with a Velocity Excess in the Core

Chapter 4

Rotor 37 Blockage Calculations

4.1 Introduction

As stated, a key feature of the tip clearance flow is the blockage that it produces. To examine this in a quantitative manner, computations of the flow in a high speed rotor (provided by Mark Celestina at the NASA-Lewis Research Center) were processed to obtain clearance blockage for a number of conditions. A brief description of the computational model used to generate the flow fields is presented below, followed by a discussion of the blockage definition and calculation method introduced by Khalid [9]. The results of the blockage calculations are also presented and compared to the trends obtained by Khalid.

4.2 Computational Procedure

Flow fields have been computed for NASA Rotor Stage 37, which is an inlet stage for a core compressor, by Suder and Celestina [18] using a three-dimensional Navier-Stokes flow solver. Parameters for this rotor are given in Table 4.1. The details of this code can be found in Adamczyk et al. [1]. The program solved a discretized, steady, Reynolds-averaged form of the equations of motion in cylindrical coordinates. The clearance flow is modeled as an orifice flow with no loss in mass, momentum and energy, as suggested by Kirtley et al. [12].

chord	2.3 in.
solidity	1.27
aspect ratio	1.19
hub/tip radius ratio	0.70
design pressure ratio	2.106
design mass flow	20.19 kg/s
inlet relative Mach number at hub	1.13
inlet relative Mach number at tip	1.48
design speed	454 m/s

Table 4.1: Parameters for NASA Rotor 37

The computational grid used had 51 cells in the radial direction, 41 cells in the circumferential direction, and 132 cells in the axial direction with 41 cells along the blade chord. Two different clearance heights were used. The low clearance case had a clearance gap spanned by two grid cells and corresponed to a clearance height of about 0.6% of the rotor tip chord. The larger clearance gap was spanned by three cells and corresponded to a clearance height of about 1% of the rotor tip chord. Suder and Celestina assumed a discharge coefficient of 0.5. This means that the computational clearance is actually half of these specified clearances (i.e. 0.3% and 0.5% of the rotor tip chord). The effect this has on the blockage calculations is discussed later in this chapter.

The clearance space was modeled by a periodic boundary condition in the clearance region, as opposed to gridding a clearance space between the blade tip and the casing. The difference between the two approaches is illustrated in Figure 4-1. Modelling the clearance gap in this way with just two or three grid cells is not enough to resolve the details of the flow in the clearance region. For this study, however, the focus is on the interaction between clearance flow and primary throughflow. The details of the flow through the clearance gap are thus less important as long as a good estimate of the gap mass flow is obtained.

Cases were run at 100% design speed and 60% design, and at various loadings using the two clearance heights. The back pressures were varied for cases ranging from below peak efficiency to peak efficiency to near stall conditions. For details on

the results of these calculations, and on similar experimental test conditions run on a test rig, see Suder and Celestina [18].

4.3 Rotor 37 Flow Fields

Before describing the blockage in the Rotor 37 solutions, the flow fields will briefly be reviewed to illustrate the essential endwall flow features that contribute to blockage. The flow fields shown in this section are the solutions for the compressor operating at near stall conditions. At this operating condition, the clearance flow structures are better defined than near the design point and, more importantly, they are the conditions of most interest. Figure 4-2 shows contours of relative total pressure in the r-theta plane at an axial location of approximately 25% chord. The figure shows roughly the upper two-thirds of the passage and focuses on the endwall region which is the region of interest for this work. The primary feature is the region of low total pressure fluid near the casing associated with the flow coming through the clearance space. This defect region will be quantified in terms of blockage later in this chapter.

Figures 4-3 through 4-5 show total pressure contour plots for axial stations at 50, 75, and 100% chord. The succession of plots (4-2 to 4-5) show the tip clearance vortex traveling across the blade passage from the suction side to the pressure side. This can also be seen in Figure 4-6 which shows the vortex trajectory. Figures 4-2 to 4-5 also show the defect area spreading out as a result of both the pressure rise and the mixing with the main passage flow. The effect of mixing out is further illustrated by noting the increasing total pressure in the core of this region.

In Figure 4-5, the defect area appears to have decreased at the exit to the blade row. This is due to the fact that the defect region has reached the pressure side of the blade before leaving the blade passage (see the vortex trajectory) and is drawn through the clearance into the neighboring blade passage. The low total pressure fluid from the blade passage on the other side can be seen near the suction surface and the endwall (the upper right corner of the figure).

The series of plots also illustrate how the suction surface boundary layer grows

through the passage. This boundary layer contributes blockage of its own, but this, as well as the smaller boundary layer on the pressure side of the blade, is not of direct interest for the present. The subsequent blockage calculations will address only the clearance related blockage.

4.4 Blockage Definition and Calculation Method

A method for quantifying blockage in axial compressors was proposed by Khalid [9]. The proposed blockage definition, which is analogous to the definition of the displacement thickness for boundary layers, is as follows:

$$A_b = \int_d \left(1 - \frac{\rho v_m}{\rho_e V_e}\right) dA \tag{4.1}$$

where

A_b = the blocked area
v_m = the velocity in the mainflow direction
ρ_e = the edge density
V_e = the edge velocity,

The subscript d indicates integration over the defect region.

The ability to evaluate this integral is dependent on two factors: (1) an identifiable mainflow direction, and (2) a substantially greater nonuniformity in the defect region such that the defect region can be identified. These two critera are generally met for typical axial compressor flow fields.

Khalid used the following as his nondimensionalized blocked area parameter:

$$\frac{A_b cos\beta_e}{\tau s / sin\beta_{vm}}. \tag{4.2}$$

where

A_b = the blocked area
β_e = the flow angle at the edge of the defect at midpitch

τ = the clearance height

s = the blade spacing

β_{vm} = the vector mean flow direction,

For details concerning this choice of nondimensionalized blockage parameter, refer to Khalid [9].

Khalid experimented with a variety of loading parameters. Two choices of loading parameter gave the best results as far as collapsing the blockage data to a single curve. The first was

$$\frac{\overline{\Delta P}^a - \overline{\Delta P_t}^a}{Q_{2\tau}} \tag{4.3}$$

where $\overline{\Delta P}^a$ and $\overline{\Delta P_t}^a$ are the differences between the area averaged pressure over the defect region and the upstream value two clearance heights from the endwall, for static and total pressures, respectively. $Q_{2\tau}$ is the value of the inlet dynamic pressure two clearances from the endwall.

The second parameter was

$$\frac{\overline{\Delta H}^a - \overline{\Delta H_t}^a}{0.5V_{2\tau}^2} \tag{4.4}$$

where the loading parameter is expressed in terms of enthalpies instead of pressures.

Khalid generated flow fields for a cantilevered stator, a General Electric E^3 Rotor B low speed rotor, and the NASA Lewis Rotor 67 transonic fan at various loadings and clearance heights. Normalized blocked area and loading parameters were calculated at 25, 50, 75, and 100% chord axial locations. From Khalid's thesis, the normalized blocked area versus pressure loading parameter is plotted in Figure 4-7, and the normalized blocked area versus enthalpy loading parameter is plotted in Figure 4-8. Plotting the data either way collapses the data, implying that the combination of the normalized blocked area and either loading parameter captures the parametric dependence of the clearance-related blockage for the flow fields Khalid examined. Comparison of Figures 4-7 and 4-8 appears to show that these loading parameters are roughly equally effective.

4.5 Clearance Modeling

As mentioned above, the clearance is modeled using a periodic boundary condition at the blade tip rather than gridding the clearance region. An important question, therefore, is what effects this modelling has on the solution. Khalid [9] addressed this issue in depth in his thesis with a central question being what physical clearance corresponds to a given computational clearance.

The issue of the difference between the computational and physical clearances becomes important when trying to relate the computational data to a physical compressor. In the normalized blockage parameter discussed above, the clearance height is used in normalizing the blocked area. For an actual compressor, it is necessary then to determine the corresponding physical clearance for the computations.

Although this consideration, strictly speaking, does not impact the results of this study, it is useful to mention the results of Khalid's assessment. He concluded that it is an acceptable approximation to equate the physical clearance to the computational clearance. This is contrary to what Suder and Celestina have assumed. For this study, therefore, one can view physical clearance as equal to computational clearance since Khalid's blockage model is being used. For more information on this issue, refer to Khalid [9] and Suder and Celestina [18].

4.6 Blockage Comparison

Calculations of blockage were carried out for 100% design speed. Attention was focused on the cases using the higher clearance (1% blade chord) since these cases produced a more defined and recognizable clearance vortex, but two low clearance flow fields, one at peak efficiency and one at a higher loading, were also examined. Normalized blockage and loading parameters were calculated using the procedure outlined by Khalid.

The normalized blocked area is plotted against the pressure loading parameter and against the enthalpy loading parameter, along with Khalid's data, in Figures 4-9

and 4-10, respectively. An interesting result is that the pressure loading parameter, which was originally derived for incompressible flow, seems to collapse the Rotor 37 cases better than the more general enthalpy loading parameter.

4.7 Effect of the Blade Shock on Blockage

To address one specific effect of compressibility on blockage, in connection with the above finding, the effect of the shock was examined. The presence of a shock (only) cannot be blamed since the Rotor 67 flow fields also possess a shock. However, blockages from these cases do not show the same differences in terms of pressure versus enthalpy loading as the Rotor 37 cases.

Figure 4-11 shows the static pressure along a streamline that is at the center of the tip clearance vortex versus the length of the core streamline. The streamlines in both cases originate at the leading edge of the rotor blade. The plot shows that the two streamlines pass through the shock at approximately the same location (about 20% chord axial location). The overall static pressure rise for the two cases is roughly the same. However, the Rotor 37 streamline experiences a larger static pressure rise due to the shock. The Rotor 67 pressure rise due to the shock is smaller, and the pressure rise is made up through blade passage diffusion. It is possible that the stronger shock is what is responsible for the difference between the plots with pressure and enthalpy loading parameters. In summary, the Rotor 37 data seems to support the pressure loading parameter as a useful parameter for predicting blockage even in high speed flows.

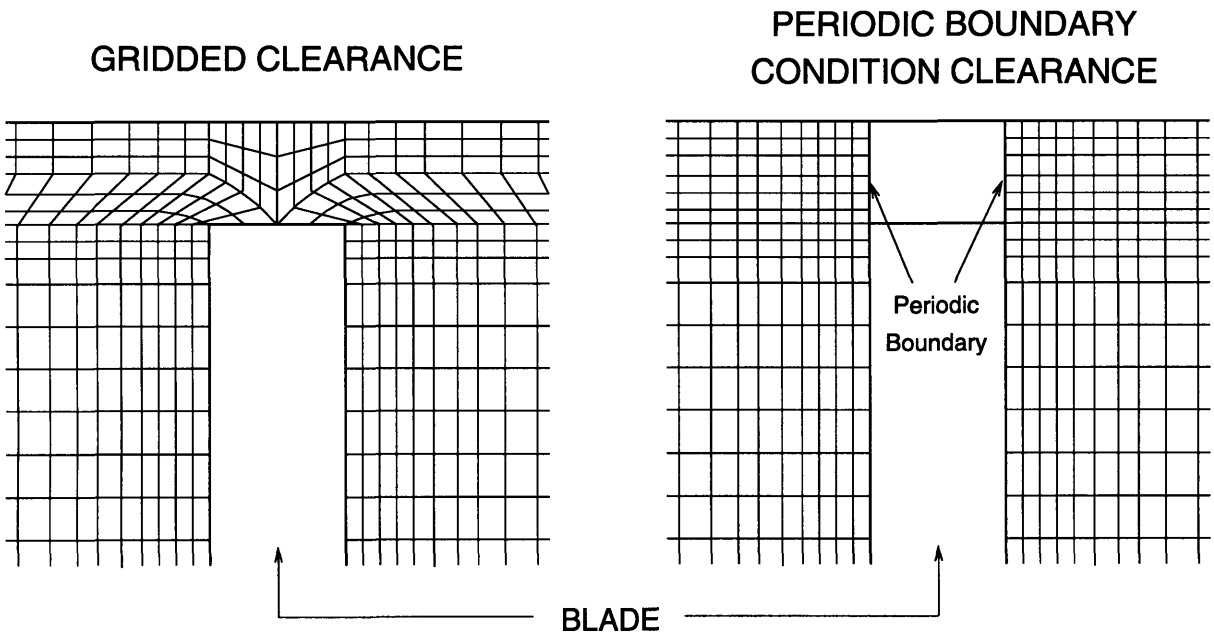

Figure 4-1: Illustration of Clearance Modelling using a Gridded Clearance and a Periodic Boundary Condition

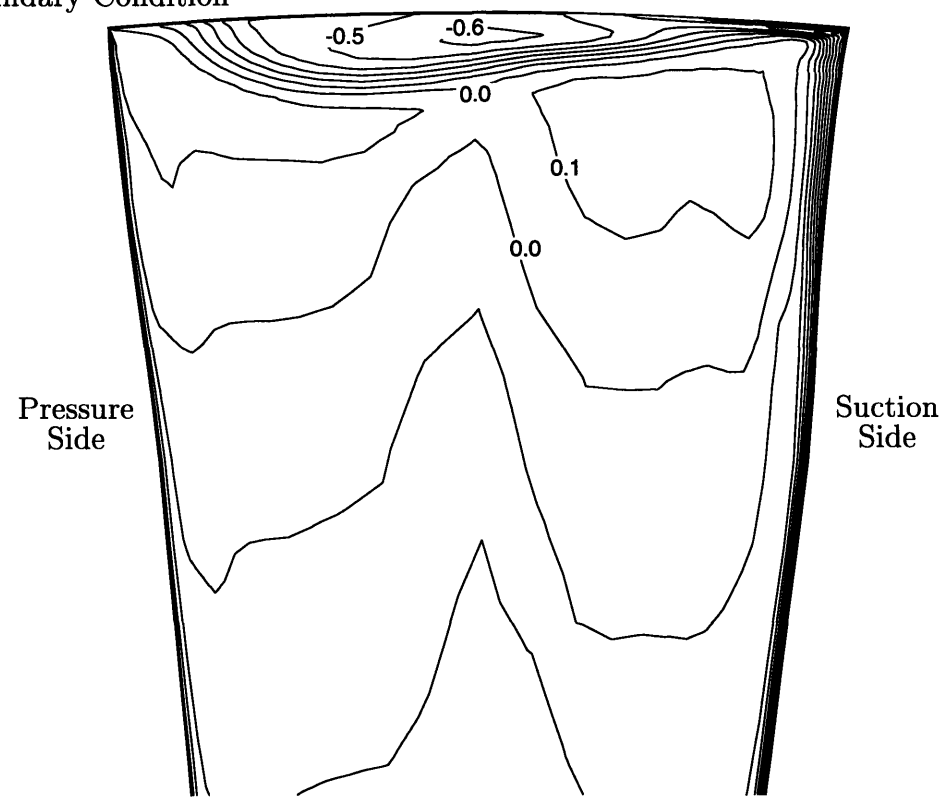

Figure 4-2: Contours of $\frac{P_t - P_{t,in}}{Q_{in}}$ at 25% Chord for Rotor 37 at Near Stall Operating Conditions

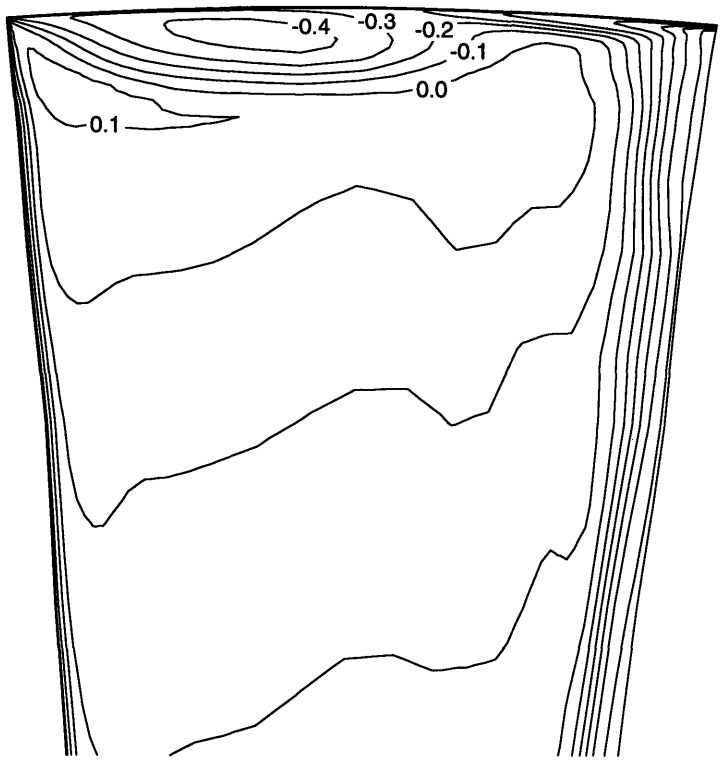

Figure 4-3: Contours of $\frac{P_t - P_{t,in}}{Q_{in}}$ at 50% Chord for Rotor 37 at Near Stall Operating Conditions

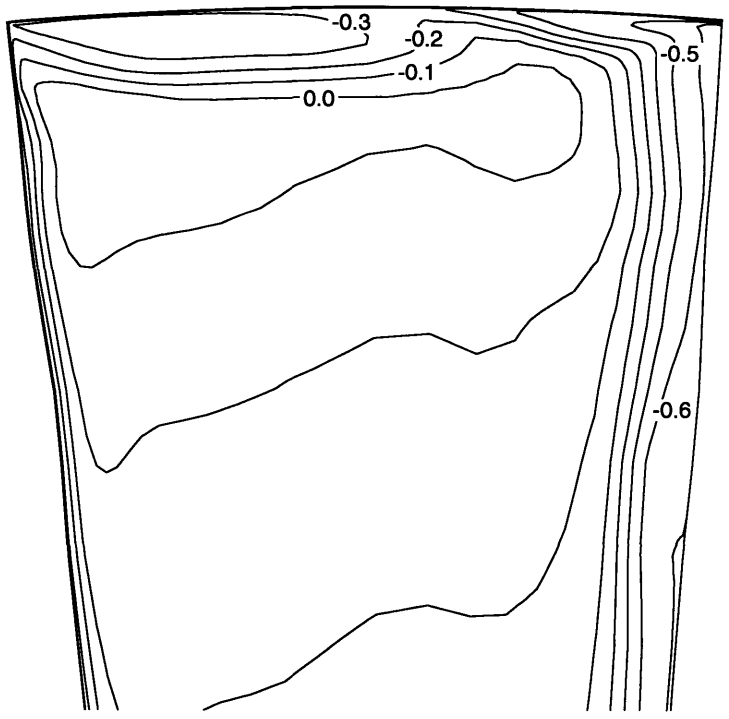

Figure 4-4: Contours of $\frac{P_t - P_{t,in}}{Q_{in}}$ at 75% Chord for Rotor 37 at Near Stall Operating Conditions

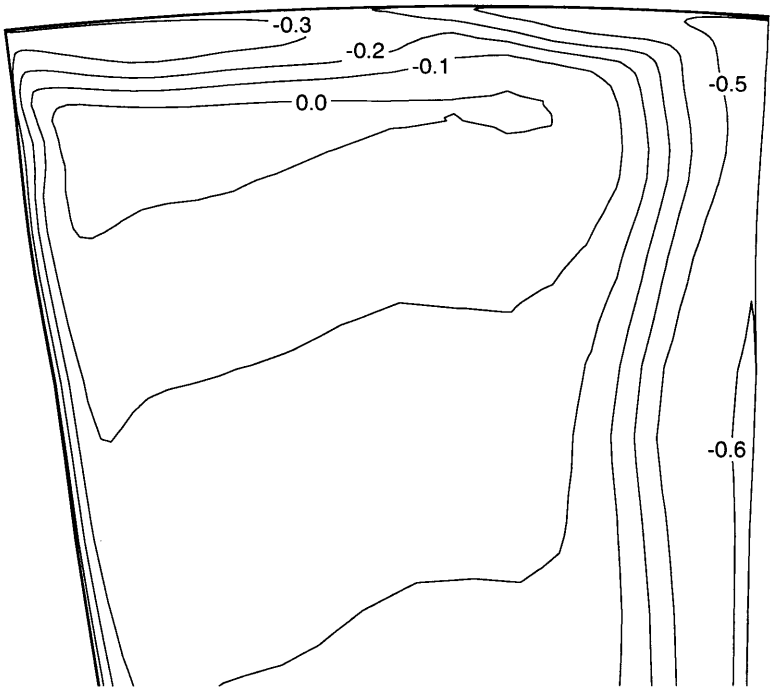

Figure 4-5: Contours of $\frac{P_t - P_{t,in}}{Q_{in}}$ at 100% Chord for Rotor 37 at Near Stall Operating Conditions

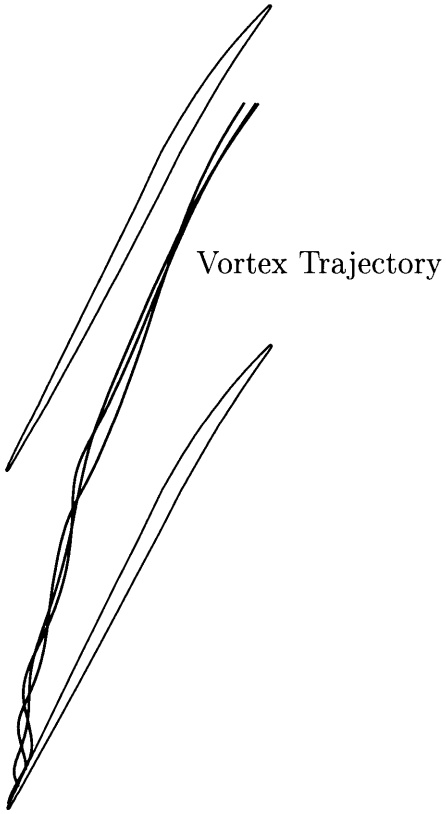

Figure 4-6: Tip Clearance Vortex Trajectory

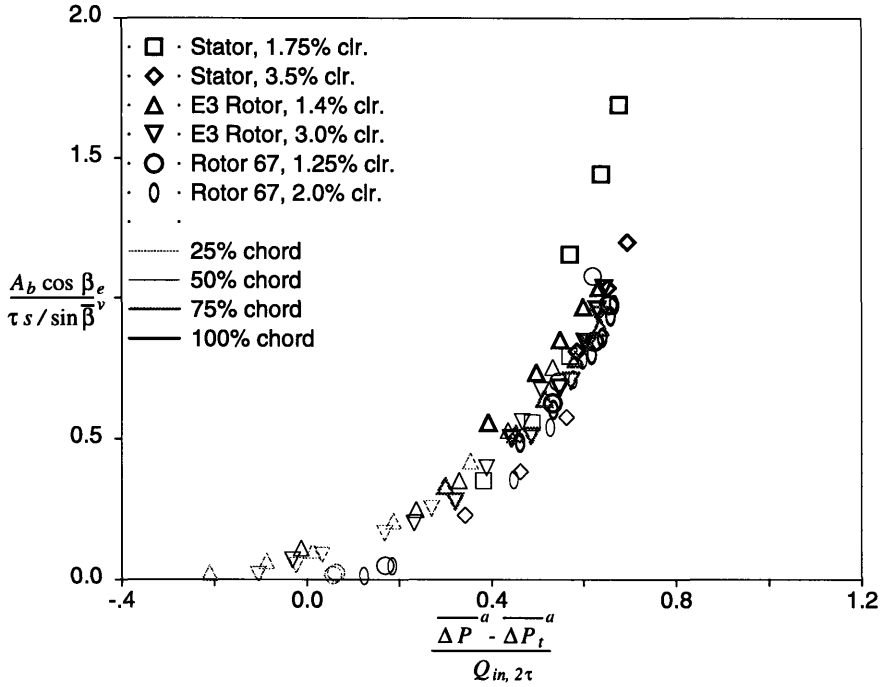

Figure 4-7: Normalized Blocked Area Versus Normalized Pressure Change for Flow Fields Calculated by Khalid

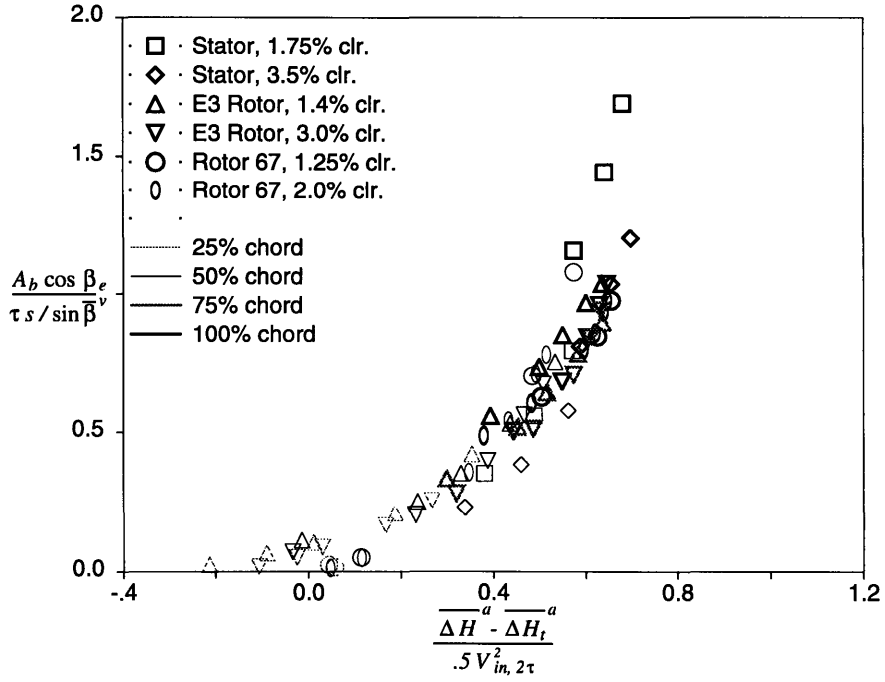

Figure 4-8: Normalized Blocked Area Versus Normalized Enthalpy Change for Flow Fields Calculated by Khalid

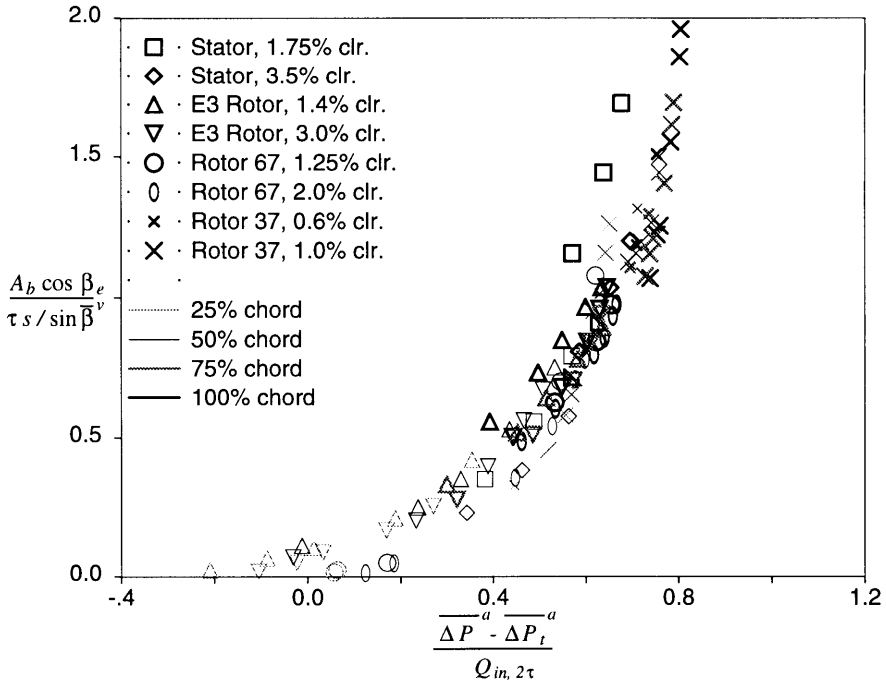

Figure 4-9: Normalized Blocked Area Versus Normalized Pressure Change Including Rotor 37 Data

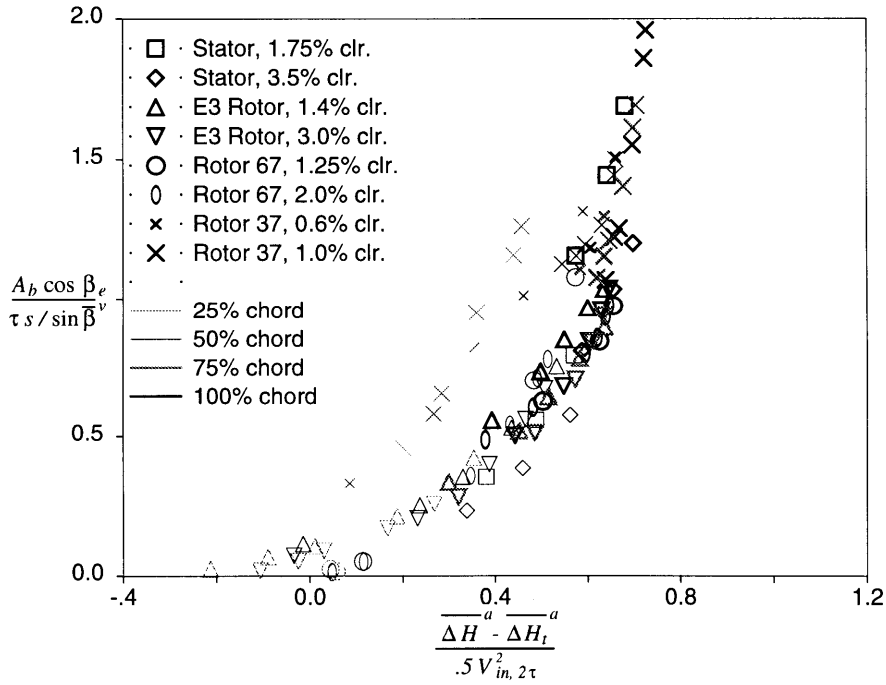

Figure 4-10: Normalized Blocked Area Versus Normalized Enthalpy Change Including Rotor 37 Data

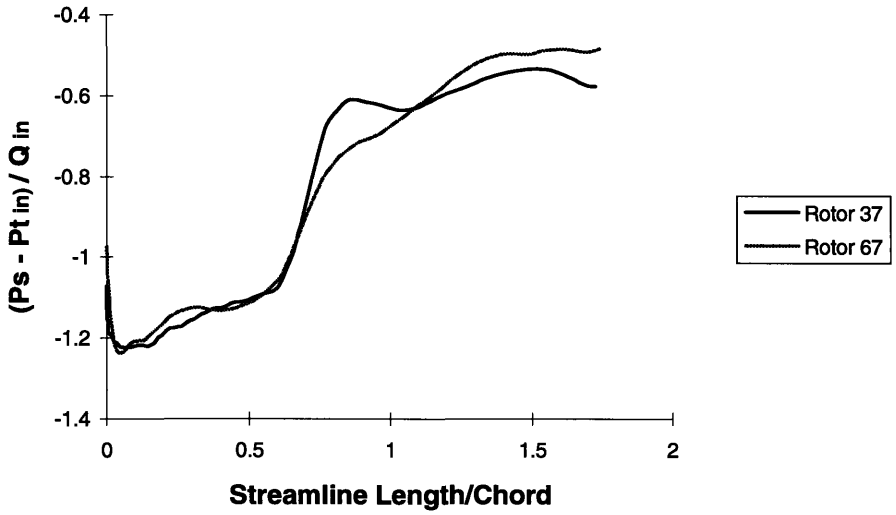

Figure 4-11: Comparison of Static Pressures along the Vortex Core Streamline for Rotor 37 and Rotor 67 Flowfields

Chapter 5

Rotor 37 Casing Treatment Calculations

5.1 Introduction

Since the 1960s, it has been known that use of casing treatment in an axial compressor can in increase the stall margin of a given machine. Casing treatment typically consists of a set of grooves or slots in the casing over the tips of the rotor blades. A variety of different configurations have been developed and tested with varying degrees of success, but one of the more effective configurations for stall suppression is the axial skewed slot. A schematic of this type of treatment is shown in Figure 5-1 (geometries used in practice generally have a rib at the mid-axial location). This form of treatment is modeled here.

An important aspect of casing treatment is the direction in which the slots are slanted. At the first level, to be effective the slot should be inclined such that the flow emerging from the slot possesses swirl opposite to the rotor rotation. Experiments by Takata and Tsukuda [19] showed that inclining the slots in the other direction reduces the stall margin of the compressor. From a slightly more incisive point of view, the work of Lee [14] showed that the increase in stable flow range correlated well with the streamwise momentum injection and that this was a desireable design feature.

While there has been much research involving casing treatment, the precise mechanism that causes the stall suppression is still in question. Two effects play a significant role. There is a removal of high loss fluid from the casing near the trailing edge, and an injection of this fluid into the flow at the front of the passage with the direction of absolute swirl reversed [16].

In this work, a computational fluid dynamic code is used to study the effects of axial skewed slot casing treatment on a high speed compressor. The focus is on the effect on blockage associated with the tip clearance flow. The goal is to quantify the blockage changes for a compressor with casing treatment and with a smooth wall.

5.2 Computational Procedure

The flow solver used to obtain the casing treatment solutions was a modified version of the code described in Chapter 4. The major modification was to the portion of the code that sets the boundary condition on the case in the blade passage. Instead of being a solid wall, no-slip boundary, the boundary was altered to allow for flow through the case. The specific form of this casing flow is described below.

The casing treatment was modeled using a method similar to that used by Crook [3]. The treatment area was defined to be the region of the casing from five percent to ninety-five percent of the axial chord in the blade passage. In the relative frame, moving with the blades, these slots move around the annulus over the blade tips. In an actual compressor, this creates an unsteady flow field in the blade passage. As discussed by Crook, however, this can be modeled using the time averaged velocity profile. Justification for this is seen in the experiments of Johnson [8].

For Crook's study, the flow from (and to) the casing treatment was set to match experimental measurements. In the present study, such measurements were not available, and two quite different flow distributions were used to parametize the problem. One was the same as used by Crook. The second, suggested by Cumpsty [4], had outflow from the treatment only in the area ahead of the shock. For the former, several different mass flows were examined.

The profile used by Crook is shown in Figure 5-2, and that suggested by Cumpsty is shown in Figure 5-3. The figures indicate only the velocity component normal to the casing.

In the suction region, the normal velocity was specified. In the injection region, in addition to the normal velocity, the r-z flow angle and the r-theta flow angle in the absolute frame, and the rothalpy were specified. The r-z flow angle was set to zero and the r-theta flow angle was set to the slot skew angle as shown in Figure 5-1. The rothalpy of the injected flow was kept equal to the rothalpy of the removed flow. While this cannot be correct (because of the work done in the relative system on the casing treatment flow), the level of stagnation temperature has only a weak effect on the results. The magnitude of the velocity profile was set by specifying the amount of mass flow that is injected and removed (the two must balance out) as a percent of the inlet mass flow. The value used by Crook was based on measurements and was for the conditions he investigated.

5.3 Overall Results and Flow Field Description

Calculations were carried out at different back pressures and casing treatment mass flows using the two different treatment profiles. All calculations were carried out with 0.5% computational tip clearance. The points examined in the computations are shown in compressor map format in Figure 5-4, and in expanded scale in Figure 5-5, which give the pressure rise (pressure ratio - 1) versus mass flow. The lowest flow point shown for the computations with the Crook casing treatment represents the near stall condition for this configuration. Below this condition converged solutions could not be obtained. On this basis, the inclusion of casing treatment shows an increase in stable flow range, as found in practice.

Additional cases were also run using only blowing and only suction in order to assess the effects of each. Table 5.1 lists parameters and conditions for each calculation.

Before addressing the parametric effects of casing treatment on blockage, a specific

Profile	$\frac{\dot{m}}{\dot{m}_{choke}}$	$\frac{\dot{m}_{c}as.tr.}{\dot{m}_{inlet}}$	P_{back}	$\pi - 1$
none	0.99291	0	1.1700	1.10034
none	0.98648	0	1.1900	1.12880
none	0.98075	0	1.2000	1.14019
none	0.95857	0	1.2200	1.15613
none	0.94152	0	1.2300	1.16325
none	0.93210	0	1.2340	1.16151
Crook	0.96927	0.035	1.2340	1.12796
Crook	0.96191	0.035	1.2540	1.15363
Crook	0.93947	0.035	1.2740	1.17792
Crook	0.91584	0.035	1.2940	1.19730
Crook	0.89618	0.035	1.3040	1.20438
Crook	0.86447	0.035	1.3140	1.20743
Cumpsty	0.96949	0.0125	1.2340	1.15170
Cumpsty	0.97100	0.025	1.2340	1.11009
blowing	0.89844	0.035	1.2340	1.16619
suction	0.99848	0.035	1.2340	1.10089
suction	0.95441	0.035	1.3000	1.18778

Table 5.1: Summary of Computed Cases

flow field will be examined in a manner similar to that of the previous chapter to see the overall effects. The case used has the same back pressure as that reviewed in Section 4.3. In Figure 5-5, this is the case with the highest mass flow of the cases run with casing treatment; the point is indicated on that figure.

Figure 5-6 shows relative total pressure contours in the r-theta plane at 25% chord. Comparing this figure to Figure 4-2 illustrates several effects due to the casing treatment. There is still a defect region associated with the flow emerging from the clearance gap, but the region is significantly smaller in area and in defect magnitude. There is also a region of high total pressure fluid directly above (closer to the casing) the defect region which appears to come from the clearance gap. The defect region has not moved as far across the blade passage as with the smooth wall. Higher total pressure fluid occupies much of the upper half of the passage, illustrating the radial extent of the casing treatment flow.

Figure 5-7 shows total pressure contours at the 50% chord axial location. Once

again, comparing this figure with the results for the smooth wall shows a smaller low total pressure region with less of a total pressure defect in the core. The figure also shows an accumulation of high total pressure fluid on the pressure surface of the blade, the fluid in this region originating from the casing treatment.

Figure 5-8 shows the 75% chord axial station, which is in the suction portion of the casing treatment. The low total pressure flow is closer to the casing because of the suction. The suction has also removed some high total pressure fluid which had accumulated on the pressure surface of the blade; what remains can be seen near the pressure surface just below the defect flow.

Figure 5-9 shows the total pressure contours at the exit to the blade passage. Compared to the smooth wall situation, the casing treatment has almost completely removed the low total pressure fluid. Visually, the overall blockage appears to have been greatly reduced. In the subsequent sections of this chapter the blockage will be quantified and compared to results for the smooth wall.

5.4 Blockage Calculations

Blockage was calculated for the flow field solutions obtained with the casing treatment modified code, and the normalized blockage parameter was plotted against both the pressure loading parameter and the enthalpy loading parameter. The results are shown in Figure 5-10 and Figure 5-11. In both plots, all the data points calculated by Khalid are denoted by small circles, and all the data points for the Rotor 37 cases without casing treatment are small x's. Once again, blockages were calculated at four axial loactions, 25%, 50%, 75%, and 100% chord.

A point to note is that at the 25% and 50% chord stations, the data points fall on the trend defined by the smooth wall data points, but they have lower ΔP_t, and hence lower blockage. Once the suction region of the casing treatment is reached, however, the data points depart from the smooth wall curve. The data at 75% and 100% chord axial locations show a large drop in blockage resulting from the clearance flow being sucked into the casing.

It can also be mentioned that the casing treatment blockages correlated more closely when plotted against the pressure loading parameter rather than the enthalpy loading parameter. Similar to the results with smooth wall, the data points from the 25% chord location had the largest departure from this trend.

5.5 Effect of Flow Injection Distribution

The flow in the casing treatment is driven by the pressure differences between the front and the rear portions of the blade passage, and it is informative to look at the pressure distribution for this rotor. This is shown in Figure 5-12 which gives static pressure contours on the casing. The static pressure is highest directly behind the shock, and one would not expect that fluid would be injected out of the casing at this location. The velocity profile used for the calculations, which is based on low speed compressor data, does not take into account the pressence of a blade shock.

It was suggested by Cumpsty [4] that a more realistic velocity profile would be one that uses the shock as the division between regions of blowing and suction. Additional computations were thus performed using the casing treatment velocity profile shown in Figure 5-3 (the blowing velocity profile was also slightly altered to prevent large velocity discontinuities in front of the shock). In these cases the casing treatment mass flow was reduced from 3.5% to 1.25% of the total inlet mass flow so that the maximum magnitude of the blowing velocity remained approximately the same as the previous casing treatment model. The back pressure was again set to the value that resulted in near stall conditions for Rotor 37 with a smooth casing.

Figures 5-13 through 5-16 show total pressure contours at the 25%, 50%, 75%, and 100% axial chord locations. The contours are qualitatively similar to the contours from the previous runs, although there are some differences. There is now a larger total pressure defect in the clearance, a slightly larger defect area at the exit to the blade passage, and little or no accumulation of high total pressure fluid on the pressure side of the blade. These differences are perhaps not unexpected given the lower casing treatment mass flow and the location of the injection.

Figure 5-17 shows the blockages from this run plotted against the normalized pressure loading parameter. Blockages from the cases highlighted in Figure 5-18 are also shown in this plot for comparison purposes. This plot further illustrates the differences mentioned above. The blockages in the rear portion of the blade passage are higher. There is also a less severe drop off in the blockage over the suction region because of the larger suction region and lower suction mass flow compared to the first injection profile.

This analysis brings up an important point in that the actual casing treatment velocity profile is not known. One velocity profile was based on data taken from a low speed, hub treated stator, and large differences between this case and the case of a high speed, case treated rotor are to be expected. The qualitative results, and the general conclusions about the effect of casing treatment on blockage from this analysis, however, should still be valid. To obtain more accurate results, detailed measurements of the flow from the casing grooves in a high speed rotor, unsteady coupled groove-mean flow field calculations, or extension of procedures for modelling the interaction using the present approach similar to those developed by Modi [15], would be useful.

5.6 Clearance Mass Flow

The clearance mass flow distribution was interrogated to see the effect of casing treatment. The clearance mass flow for the cases (with and without Crook's casing treatment) has been plotted against the static pressure parameter $\frac{\Delta P}{Q_{inlet}}$, defined as change in casing static pressure at midpitch, inlet to exit, normalized by the area averaged dynamic head at the inlet to the computational domain, in Figure 5-19. The figure shows that the clearance mass flow, i.e. the integral of ρV_{normal} over the clearance, approximately doubles with the addition of casing treatment for the Crook profile. The analysis of cases using Cumpsty's profile will be shown subsequently.

Figures 5-20 and 5-21 show how the clearance mass flow is distributed with distance along the blade for cases without and with casing treatment, respectively. The

vertical axis of these plots is:

$$\frac{\frac{1}{dl}\rho V_n dA}{\frac{1}{c}\iint \rho V_n dA} \tag{5.1}$$

where dl is the incremental distance along the chord, V_n is the velocity normal to the blade, c is the chord, dA is the clearance area corresponding to the increment dl, and the quantity is evaluated at axial stations along the chord. The quantity in the numerator is essentially the incremental clearance mass flow per unit chord increment, and the quantity in the denominator is the total clearance mass flow per unit chord.

Figures 5-20 and 5-21 show that the casing treatment causes a large increase in the clearance mass flow over the (front) portion of the blade corresponding to the location of the blowing region from the casing treatment. The casing treatment is injecting fluid directly into the clearance space on the pressure side of the blade.

This point is shown from another aspect by examining the total pressure distribution of the clearance flow as in Figures 5-22 and 5-23. The figures show mass average total pressure across the clearance (i.e. the mass average over the radial extent of the clearance) versus chord. The total pressure corresponding to the region of high clearance mass flow is much higher than inlet, indicating that this portion of the clearance flow originates from the casing treatment flow.

One can also examine that portion of the clearance mass flow which does not have this high value. This is done in Figure 5-24 which shows the portion of the clearance flow with total pressure equal to or below the inlet value. The magnitude is a little more than half of the clearance mass flows from the smooth wall cases. Figure 5-25 shows the clearance mass flow distributions without the high total pressure fluid. This figure indicates that in the region from about 5% to 50% chord, all of the clearance flow originated from the casing treatment injection. High total pressure fluid from the casing treatment flow thus fills the clearance in the blowing region of the casing treatment, and ends up in the core of the clearance vortex. The suction portion of the casing treatment flow does not directly affect the flow that comes through the

clearance, but instead acts on the tip clearance vortex in the passage. The suction removes this high loss fluid from the main passage flow.

Performing this same analysis on the cases using the Cumpsty casing treatment velocity profile shows a similar effect. Figure 5-26 and Figure 5-27 show clearance mass flow and total pressure distributions, respectively, for the two cases (with treatment mass flows of 1.25% and 2.5% of inlet mass flow). Figure 5-26 shows a higher clearance mass flow over the front portion of the chord for the 1.25% case compared to the 2.5% case. This is presumably due to the higher suction over the clearance for the 2.5% clearance mass flow case. The figures show that over a portion of the chord there is high total pressure fluid emerging from the clearance. Figure 5-28 shows the clearance mass flow distribution neglecting this high total pressure fluid. A plot of total clearance mass flow and of clearance mass flow without the high total pressure fluid, versus the static pressure rise, is shown in Figure 5-29. The effect is not as large as with the low speed velocity distribution, due to the lower casing treatment mass flows and the location of the blowing region.

5.7 Effects of Blowing and Suction on Blockage

In an attempt to isolate the effects of flow injection and removal, two additional runs were performed, one with blowing only and another with suction only. The blockages were calculated in the same manner as for the previous cases at the same axial chord locations, and these blockages are plotted versus pressure loading parameter in Figure 5-30. Several points, which were chosen because of their close proximity on the speedline plot, are highlighted for further discussion, and these are shown in Figure 5-31 and were chosen because of their close proximity on the speedline plot.

With blowing, there is a decrease in the level of blockage compared to smooth wall as a result of the effects descibed in the previous section. Compared to the full casing treatment, the reduction in blockage is not as large and there is no drop off in the blockage over the rear portion of the blade passage (these differences are to be expected since there is no flow removal present).

With suction, the blockage trend through the blade passage shows a reduction in blockage in the front of the passage similar to the blowing case, but there is a large drop in blockage over the rear portion of the blade passage, closely resembling the blockage trend from the full casing treatment run. This implies that flow removal from the rear of the of the blade passage is dominant in blockage reduction from casing treatment. The presence of blowing in the front portion of the passage does effect the blockage, but its effects appear to be overshadowed by the effects of the suction. This is contrary to the result obtained by Lee [14]. Lee experimentally examined the effect of flow injection and flow suction on the stall margin of an axial compressor blade row. Both flow injection and removal increased the stalling pressure rise, but neither was as effective as wall treatment.

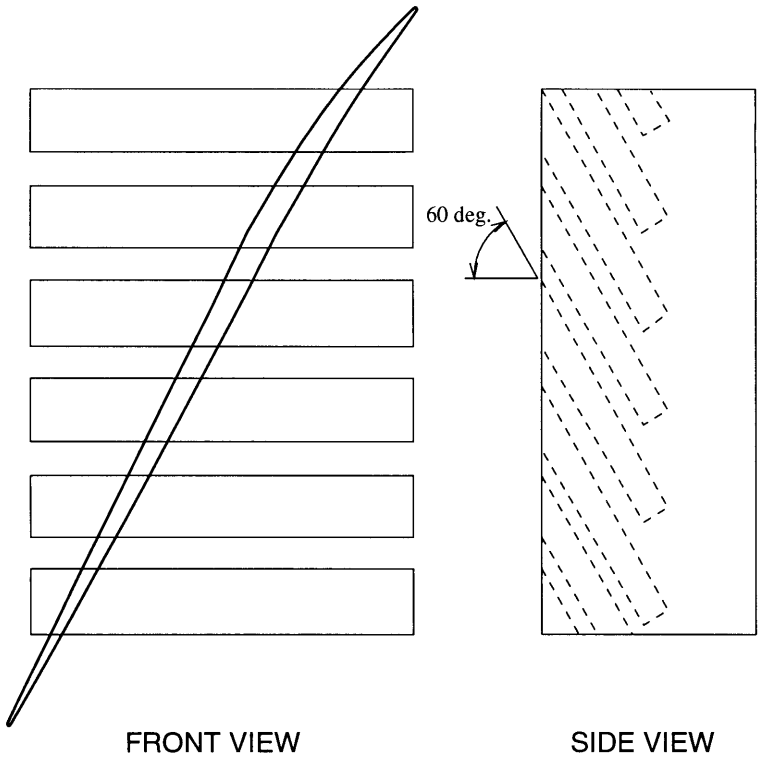

Figure 5-1: Schematic of Axial Skew Slot Treatment

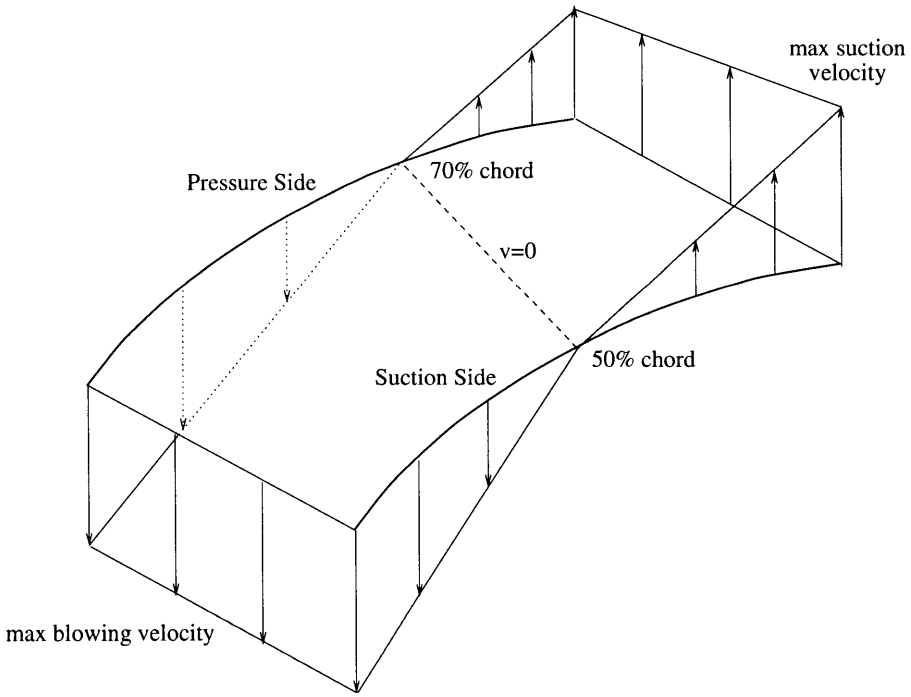

Figure 5-2: Time Averaged Casing Treatment Radial Velocity Profile (Crook)

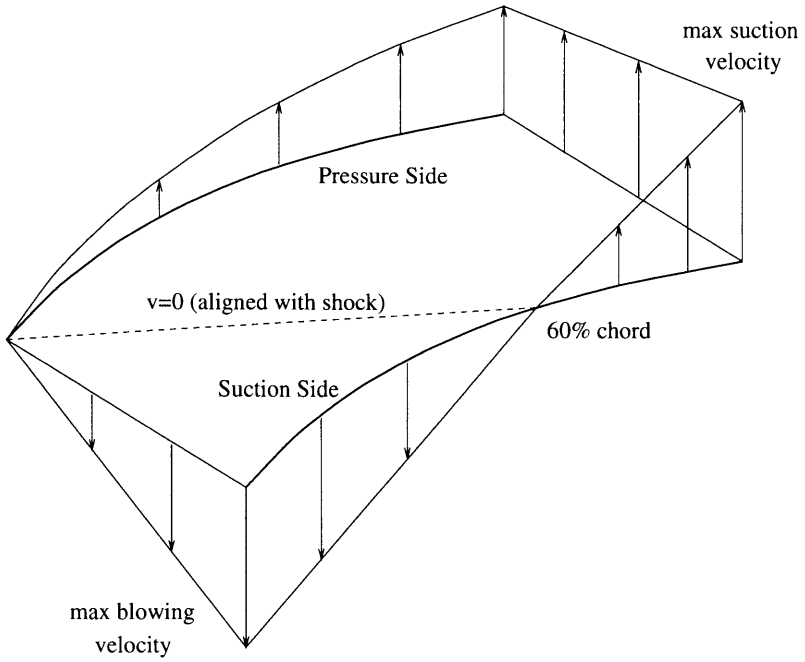

Figure 5-3: Time Averaged Casing Treatment Radial Velocity Profile (Cumpsty)

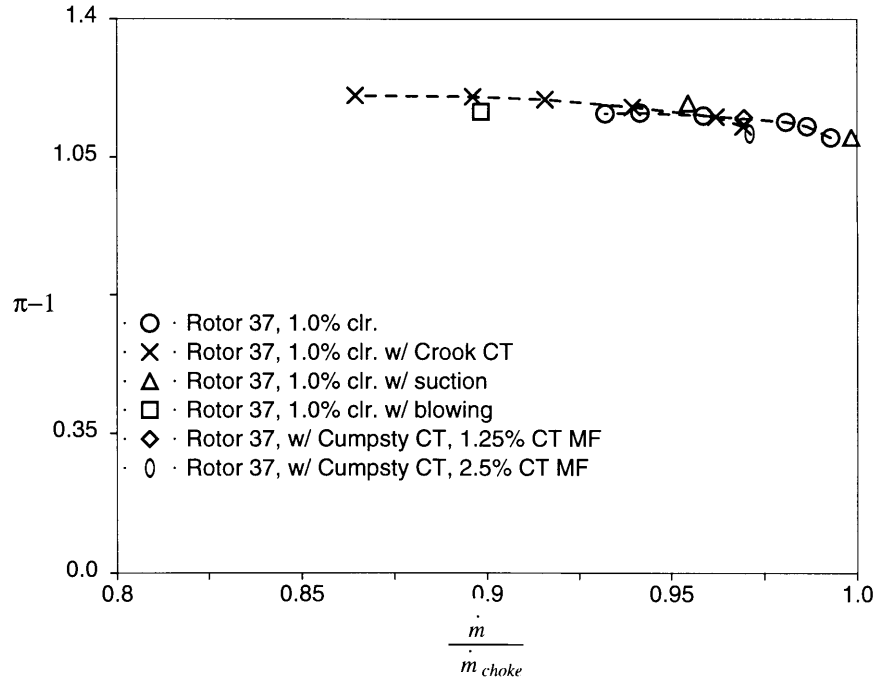

Figure 5-4: Computations Carried Out for Rotor 37 With and Without Casing Treatment (MF = Mass Flow)

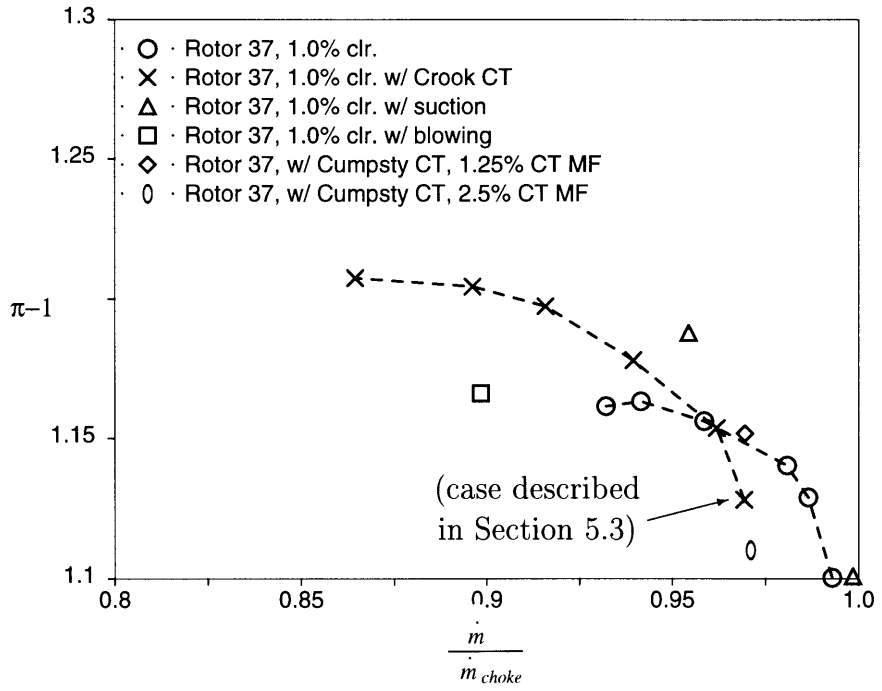

Figure 5-5: Speedlines for Rotor 37 With and Without Casing Treatment

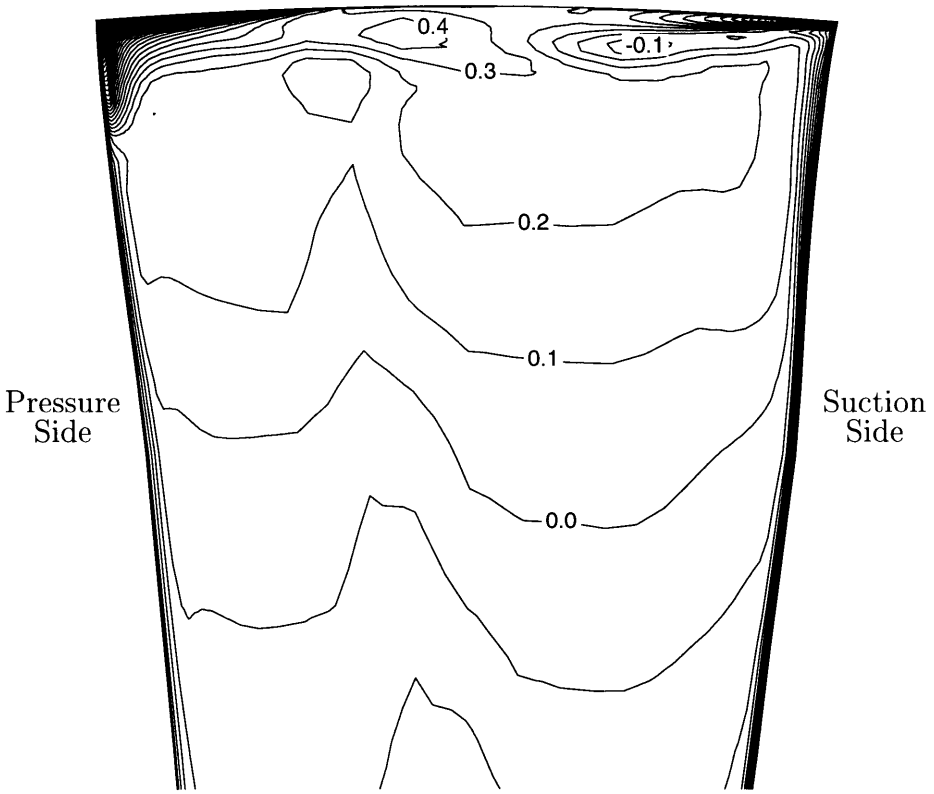

Figure 5-6: Contours of $\frac{P_t - P_{t,in}}{Q_{in}}$ at 25% Chord for Rotor 37 With Crook Casing Treatment

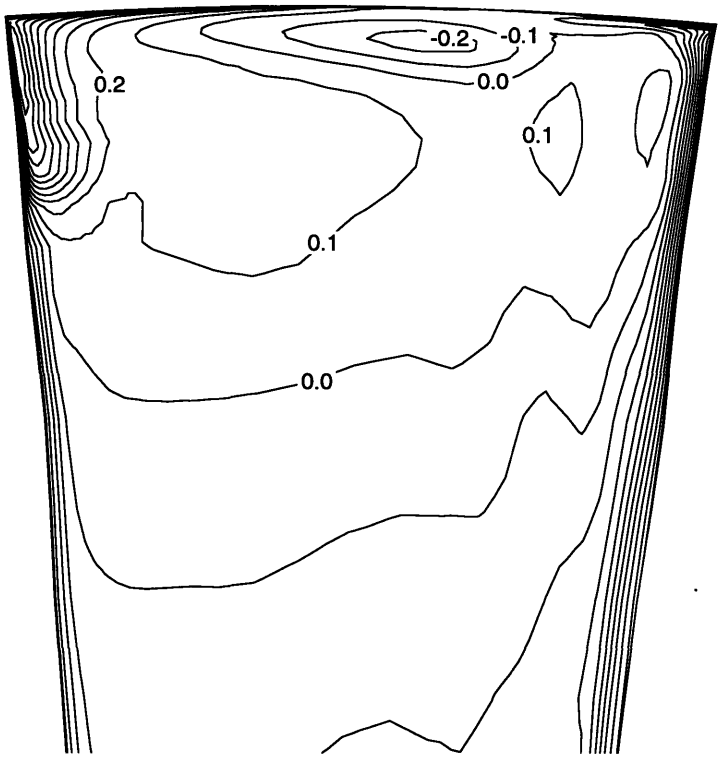

Figure 5-7: Contours of $\frac{P_t - P_{t,in}}{Q_{in}}$ at 50% Chord for Rotor 37 With Crook Casing Treatment

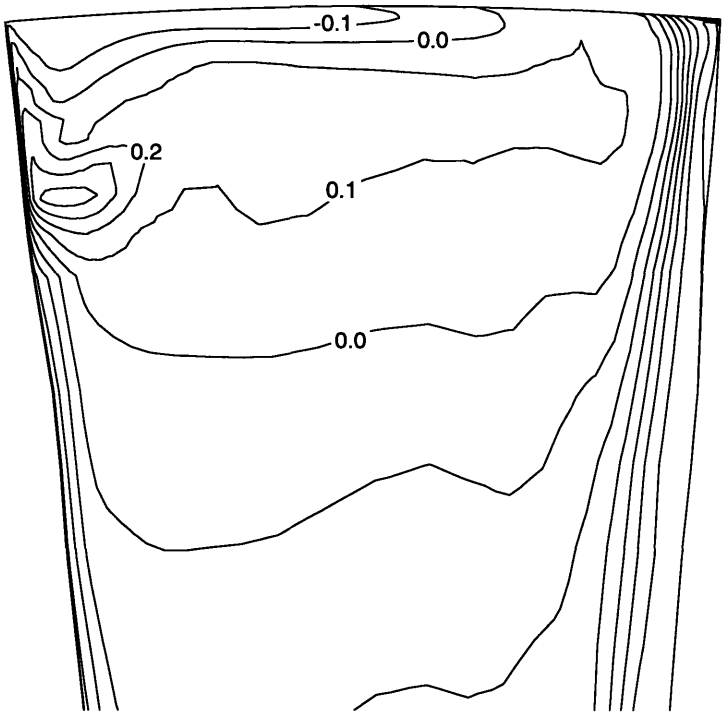

Figure 5-8: Contours of $\frac{P_t - P_{t,in}}{Q_{in}}$ at 75% Chord for Rotor 37 With Crook Casing Treatment

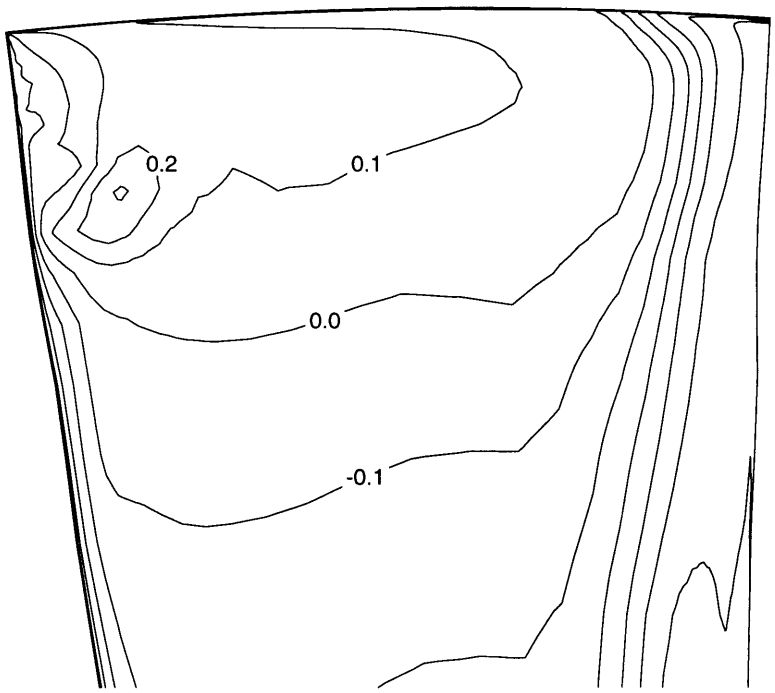

Figure 5-9: Contours of $\frac{P_t - P_{t,in}}{Q_{in}}$ at 100% Chord for Rotor 37 With Crook Casing Treatment

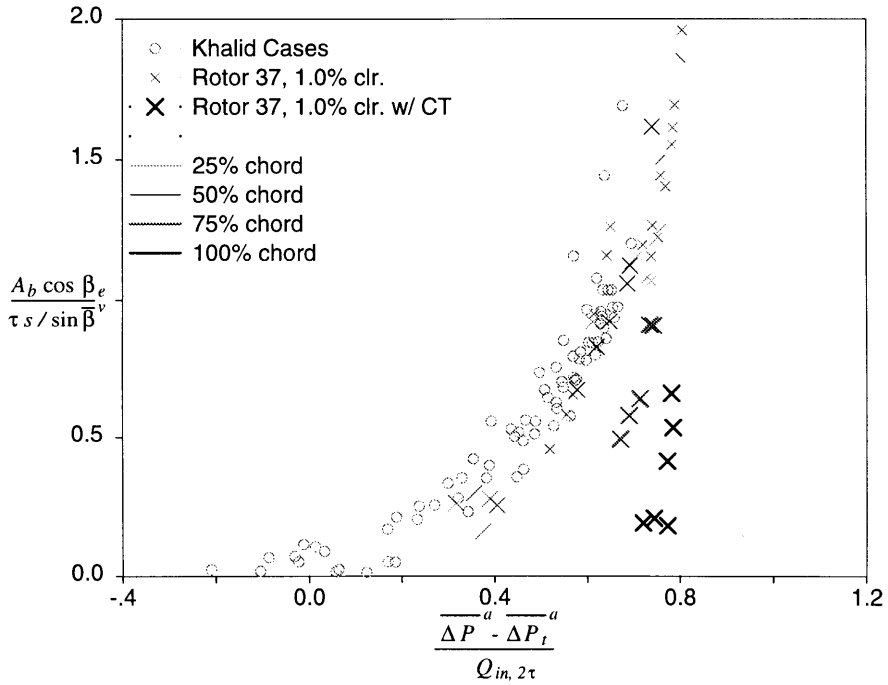

Figure 5-10: Normalized Blocked Area Versus Normalized Pressure Change for Rotor 37 With Crook Casing Treatment

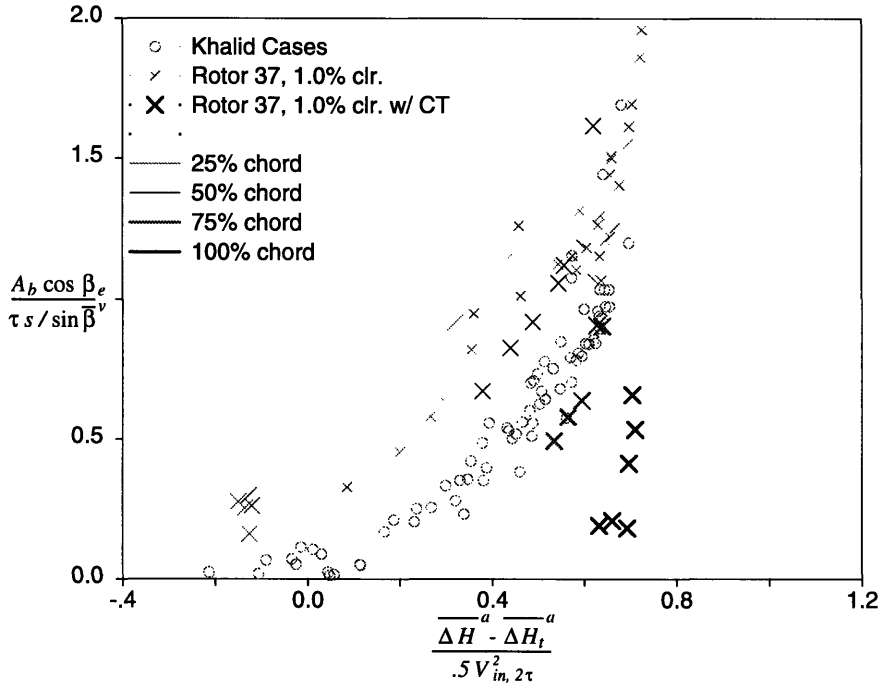

Figure 5-11: Normalized Blocked Area Versus Normalized Enthalpy Change for Rotor 37 With Crook Casing Treatment

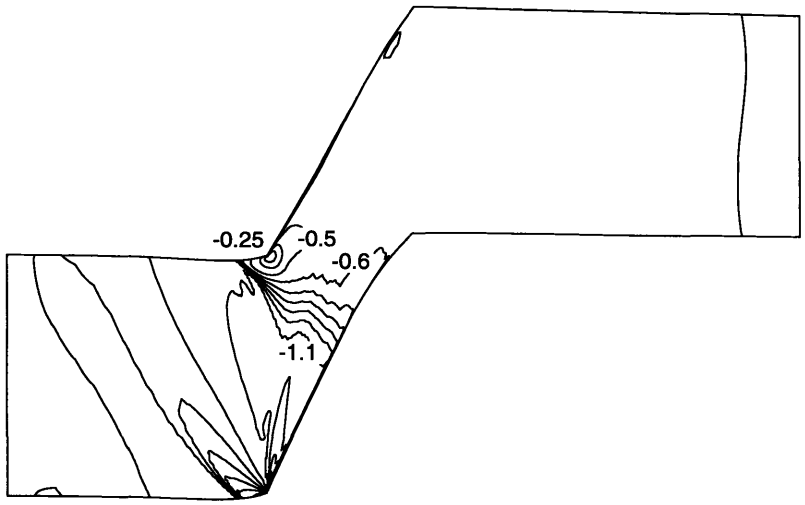

Figure 5-12: Contours of $\frac{P_s - P_{t,in}}{Q_{in}}$ on the Casing for Rotor 37

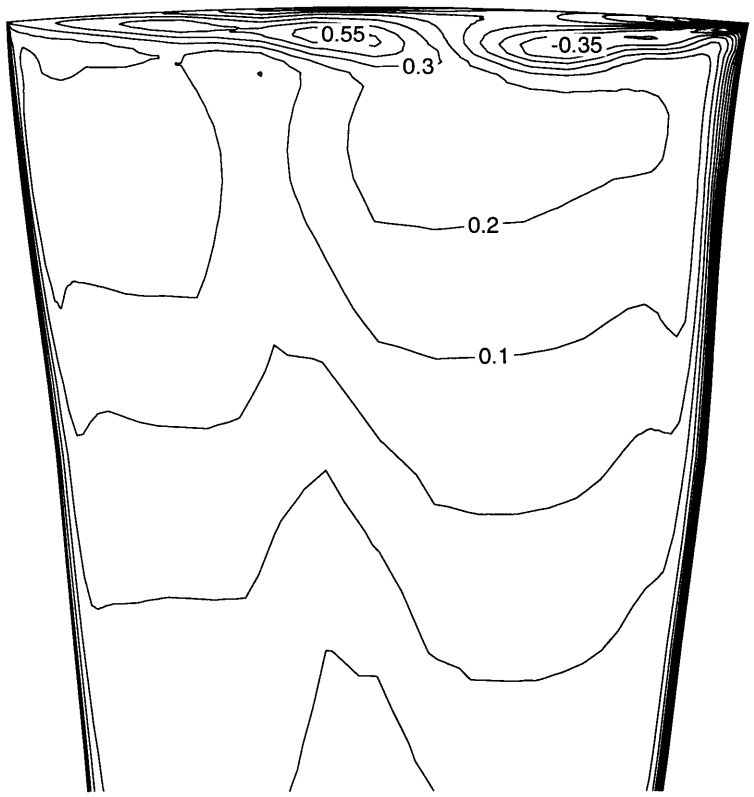

Figure 5-13: Contours of $\frac{P_t - P_{t,in}}{Q_{in}}$ at 25% Chord for Rotor 37 With Cumpsty Casing Treatment

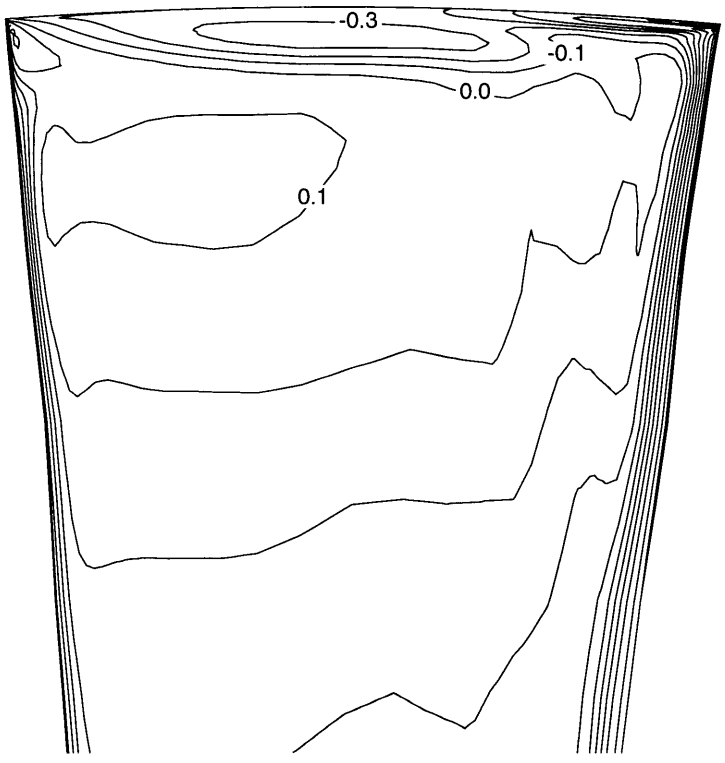

Figure 5-14: Contours of $\frac{P_t - P_{t,in}}{Q_{in}}$ at 50% Chord for Rotor 37 With Cumpsty Casing Treatment

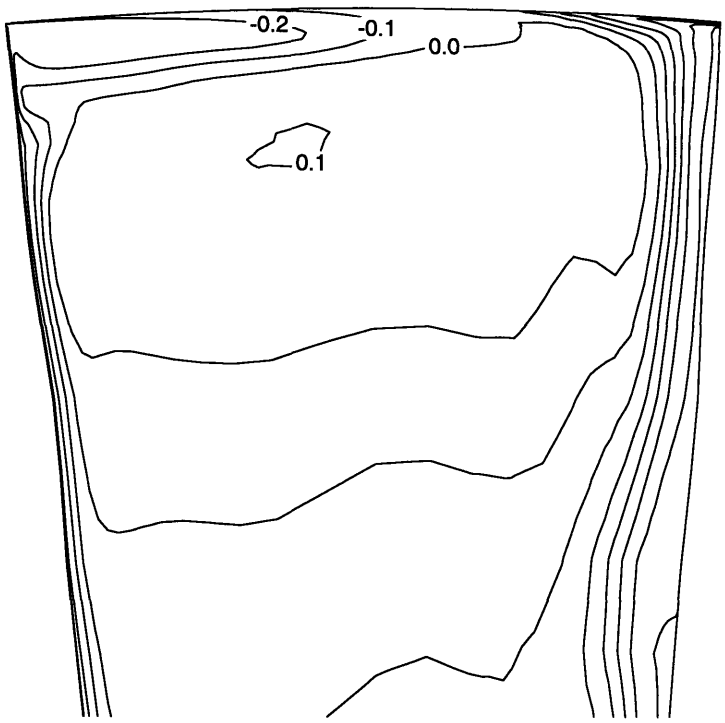

Figure 5-15: Contours of $\frac{P_t - P_{t,in}}{Q_{in}}$ at 75% Chord for Rotor 37 With Cumpsty Casing Treatment

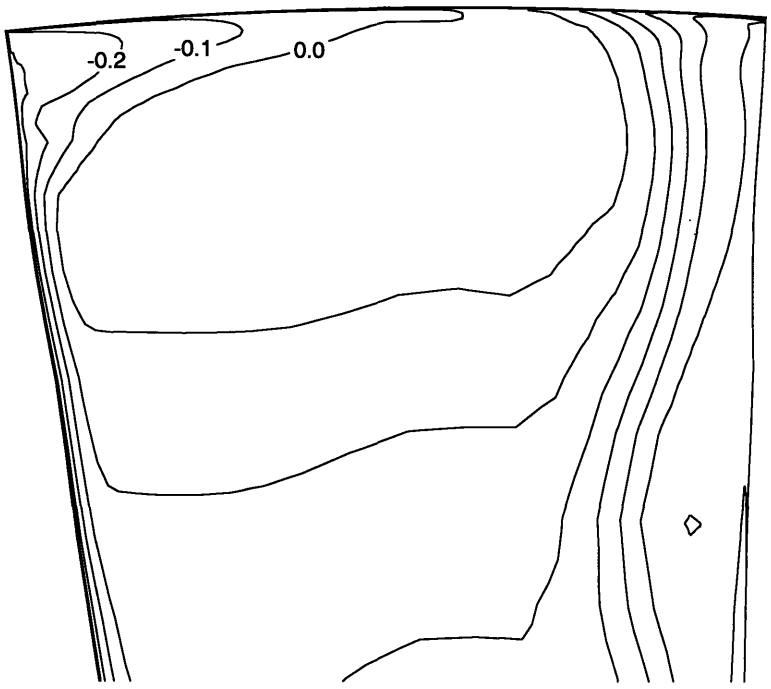

Figure 5-16: Contours of $\frac{P_t - P_{t,in}}{Q_{in}}$ at 100% Chord for Rotor 37 With Cumpsty Casing Treatment

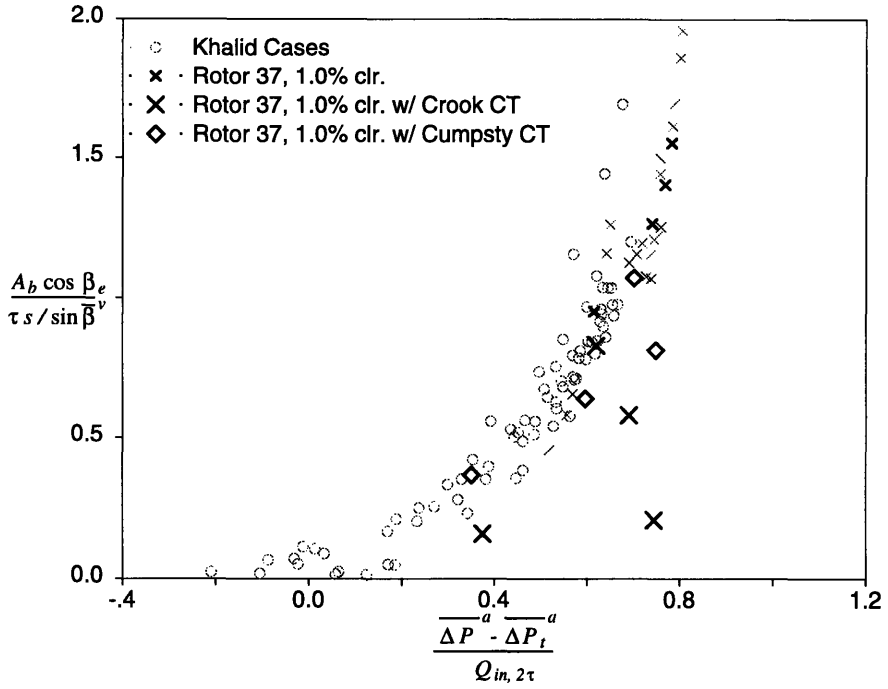

Figure 5-17: Normalized Blocked Area Versus Normalized Pressure Change for Rotor 37 With Cumpsty Casing Treatment

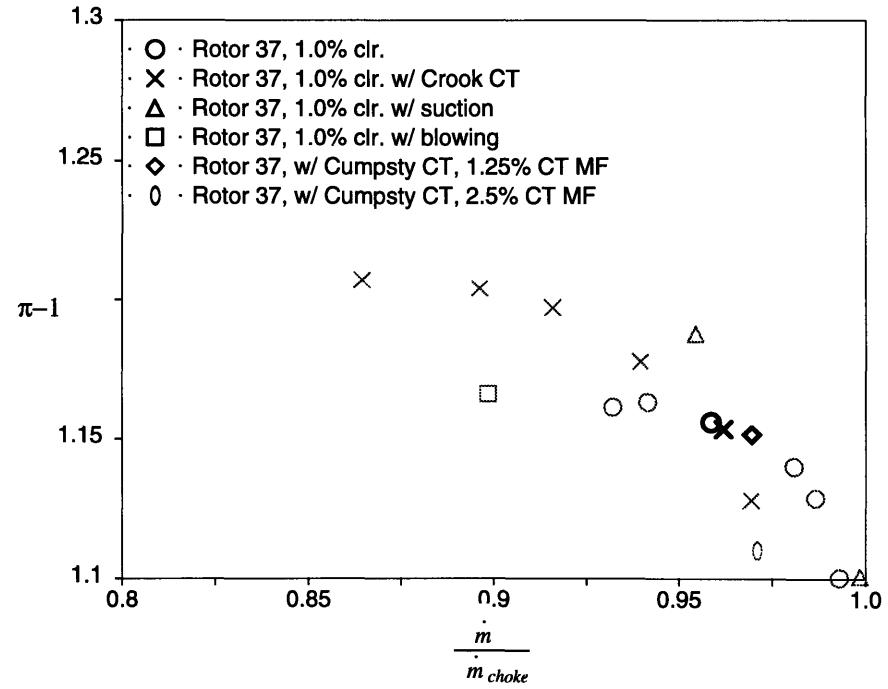

Figure 5-18: Highlighted Cases for Cumpsty Casing Treatment Blockage Analysis

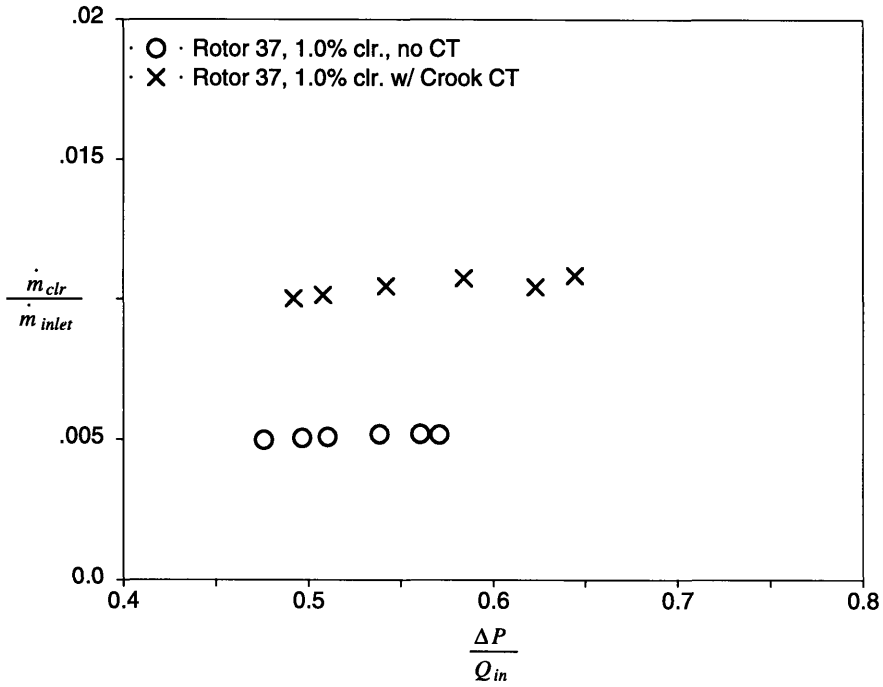

Figure 5-19: Clearance Mass Flow Versus Loading for Rotor 37 With and Without Crook Casing Treatment

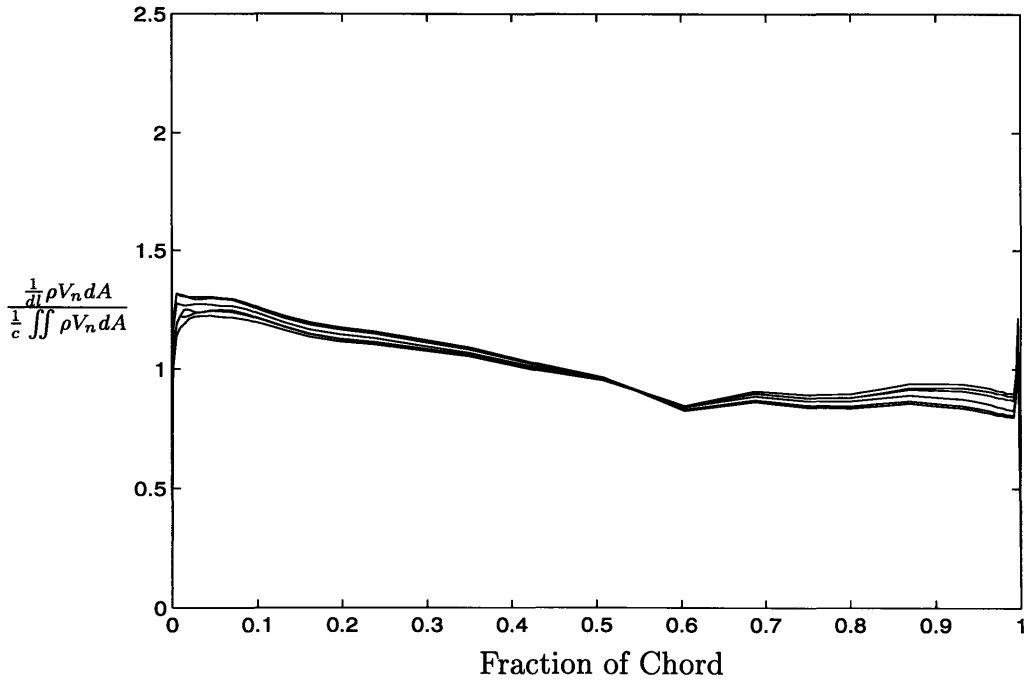

Figure 5-20: Clearance Mass Flow Distribution along the Chord Without Casing Treatment

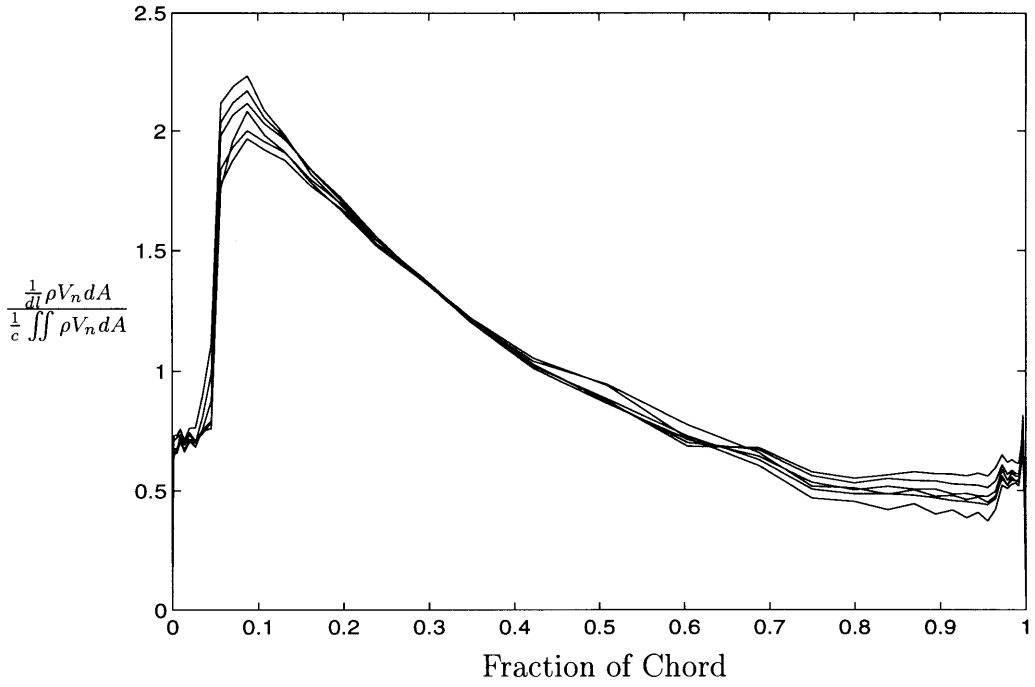

Figure 5-21: Clearance Mass Flow Distribution along the Chord With Crook Casing Treatment

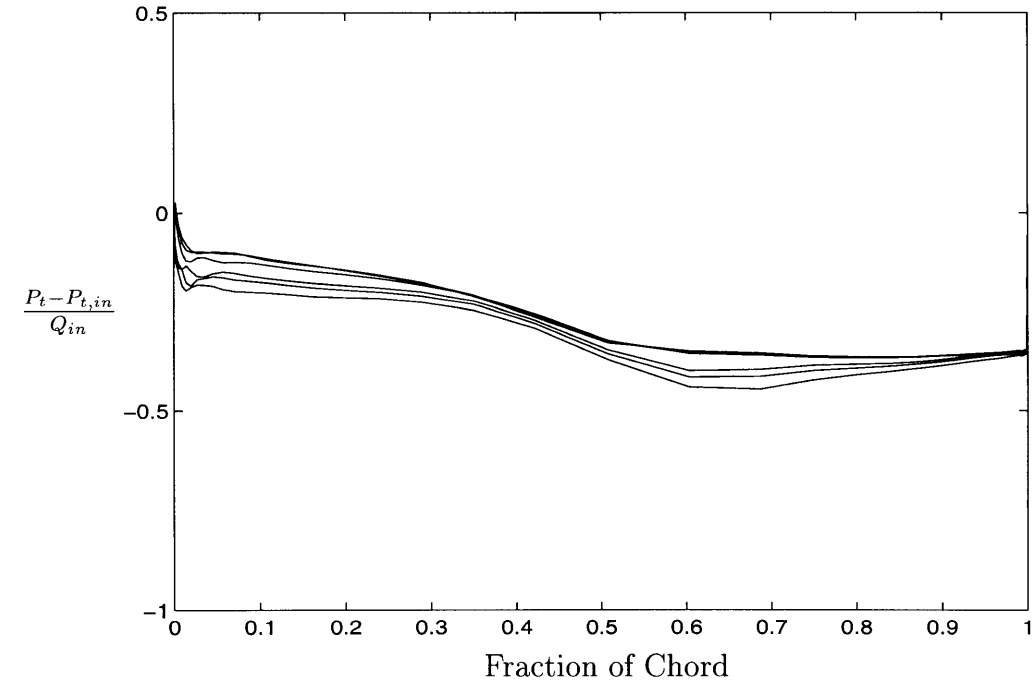

Figure 5-22: Clearance Total Pressure Distribution along the Chord Without Casing Treatment

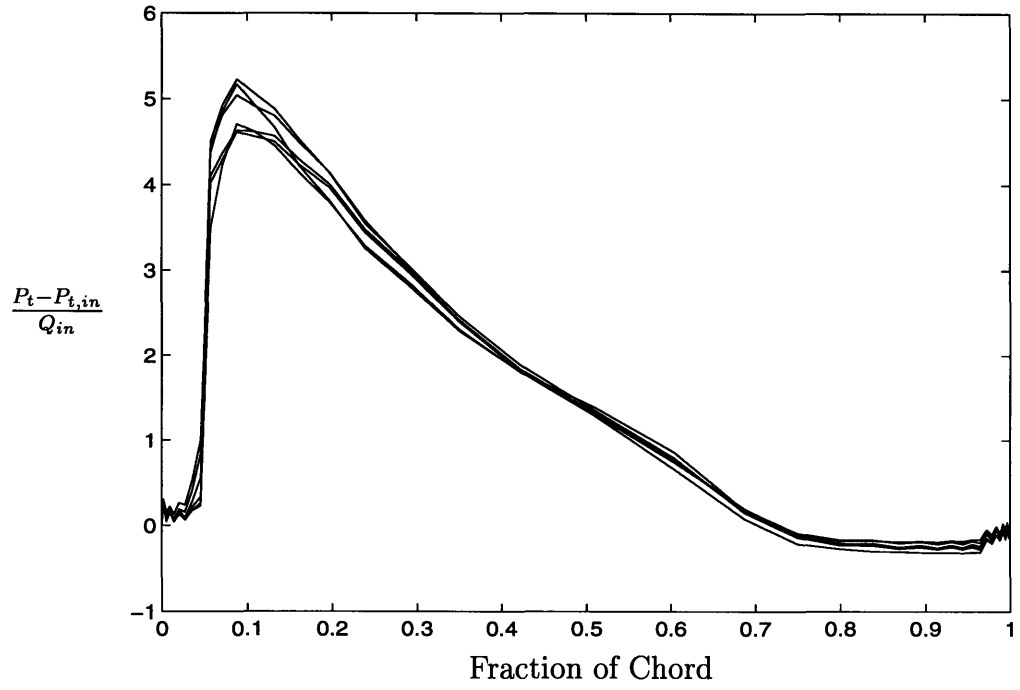

Figure 5-23: Clearance Total Pressure Distribution along the Chord With Crook Casing Treatment

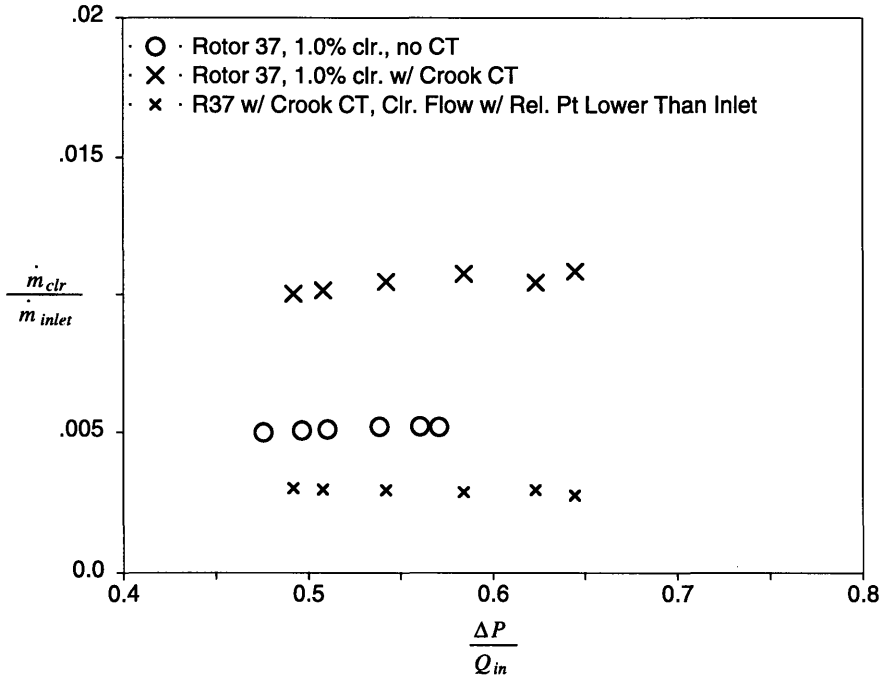

Figure 5-24: Clearance Mass Flow Versus Loading for Rotor 37 With and Without CrookCasing Treatment

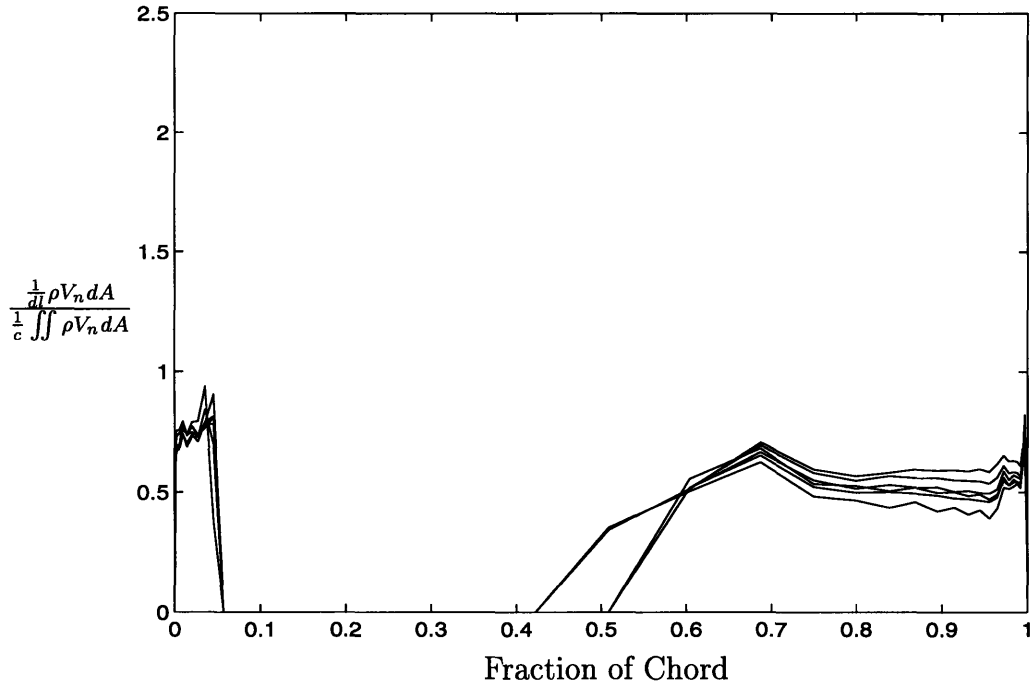

Figure 5-25: Clearance Mass Flow Distribution along the Chord With Crook Casing Treatment Neglecting High Total Pressure Fluid

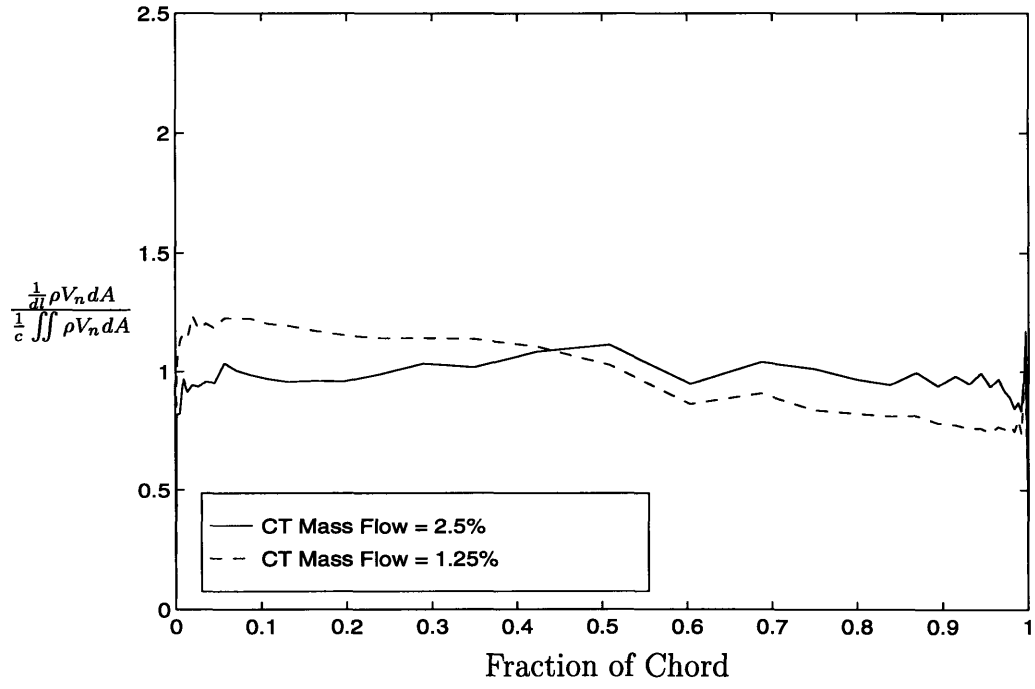

Figure 5-26: Clearance Mass Flow Distribution along the Chord With Cumpsty Casing Treatment

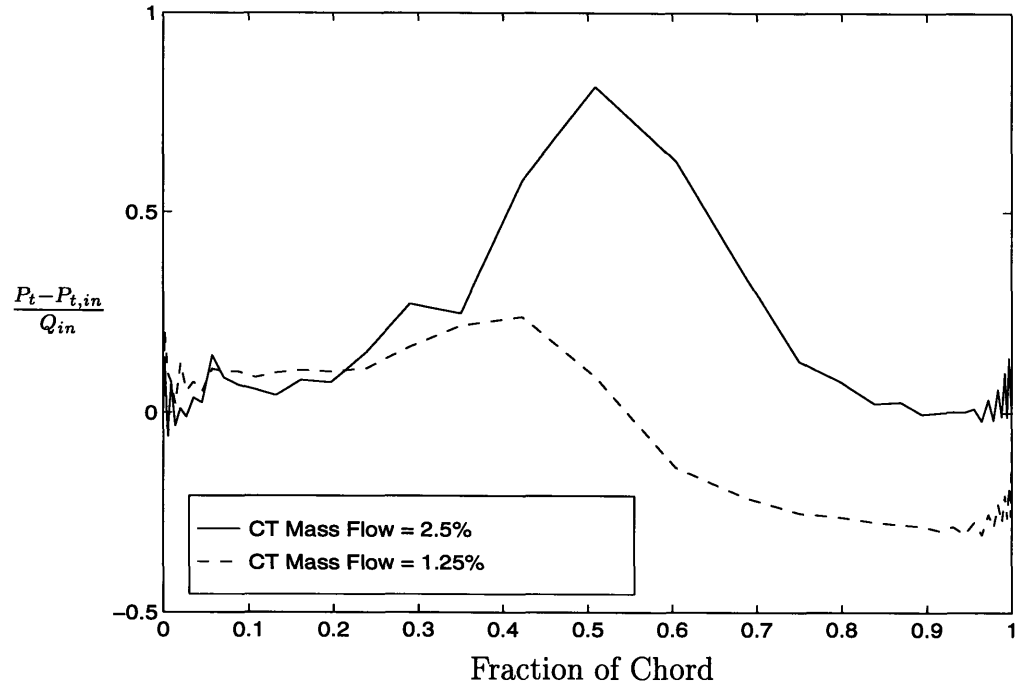

Figure 5-27: Clearance Total Pressure Distribution along the Chord With Cumpsty Casing Treatment

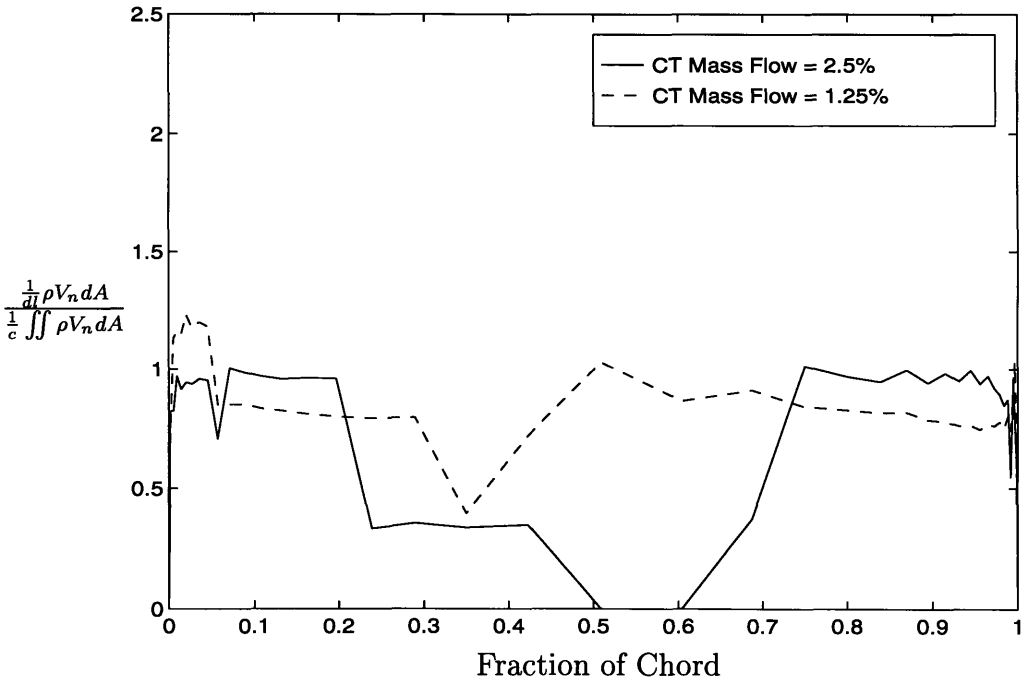

Figure 5-28: Clearance Mass Flow Distribution along the Chord With Cumpsty Casing Treatment Neglecting High Total Pressure Fluid

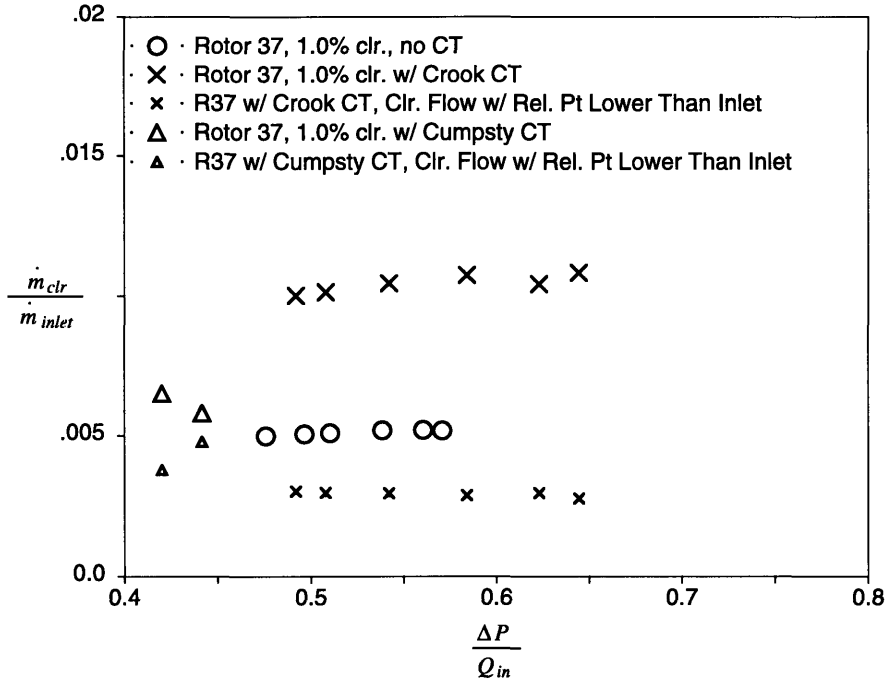

Figure 5-29: Clearance Mass Flow Versus Loading for Rotor 37 With and Without Casing Treatment

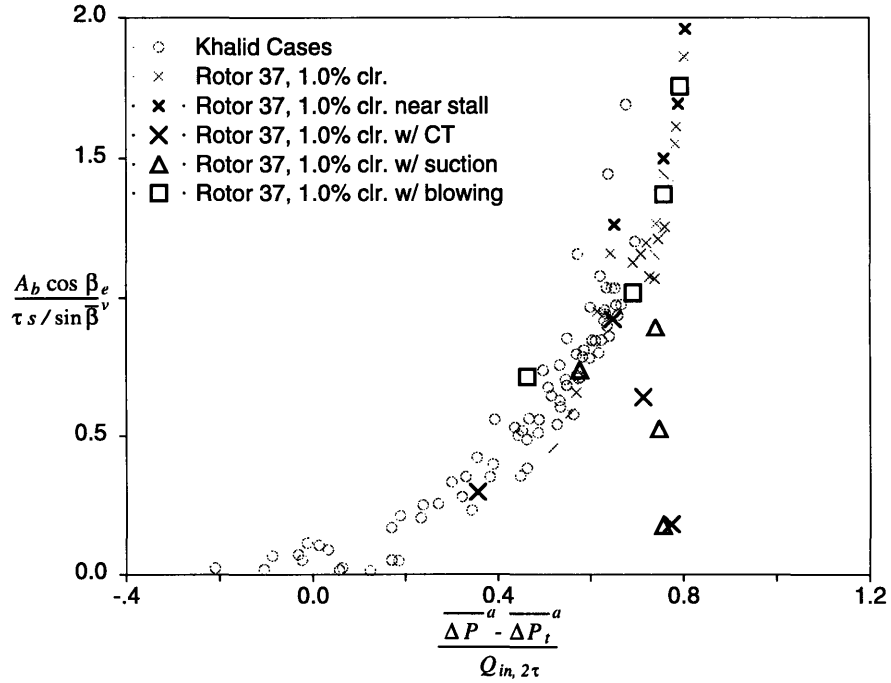

Figure 5-30: Normalized Blocked Area Versus Normalized Pressure Change for Rotor 37 With Just Blowing and Just Suction

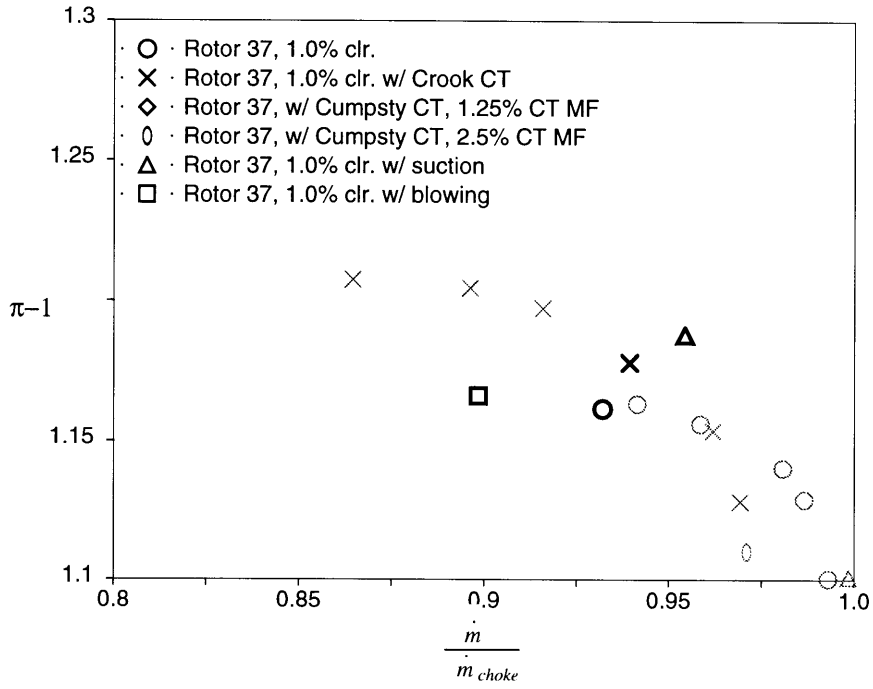

Figure 5-31: Highlighted Cases for Blowing and Suction Blockage Analysis

Chapter 6

Conclusions

6.1 Summary of Results and Conclusions

- An experimental investigation was performed to examine the effect of core stagnation pressure on the behavior of a vortex in a pressure rise similar to that encountered in an axial compressor. The capability to withstand a pressure rise without a large expansion in vortex core area is strongly dependent on this quantity. Results were in agreement with the quasi one-dimensional model of Khan [11].

- A computational study was carried out of the three-dimensional flow in a high speed axial compressor rotor (NASA Rotor 37). The results were used to assess trends in blockage with loading parameters using the framework proposed by Khalid [9]. Modifications were made to the code to model the effects of casing treatment on a compressor rotor (the casing treatment was modeled in a manner similar to that employed by Crook [3]).

- The casing treatment calculations showed a reduction in blockage and an increase in the flow range at which solutions could be obtained compared to smooth wall.

- Casing treatment flow injection resulted in blockage reduction by directly af-

fecting the clearance flow. The fluid on the pressure surface of the blade was prevented from entering the clearance, so that the fluid that does emerge and roll up into the clearance vortex has a higher total pressure than with no casing treatment.

- The suction part of the casing treatment resulted in the removal of low total pressure fluid from the rear portion of the blade passage, near the endwall. This flow removal caused a large drop in the blocked area in the rear of the blade passage.

- The casing treatment velocity profile was also varied to assess the effect of the passage shock. The results had the same trend as the casing treatment velocity distribution derived from low speed data, but the effects on the clearance mass flow and blockage were much less marked.

- Computations using blowing and suction alone showed that both flow injection and flow removal contribute to reducing blockage in a compressor with casing treatment, but it appeared that the suction was the dominant effect.

Appendix A

Sample Data Traverses

A.1 Upstream Data

The following are samples of initial swirl angle profiles. Figures A-1, A-2, and A-3 are from the cases with vane angles set to 5, 10, and 15 degrees, respectively, with no core injection. In all figures, r is the local radius, and R is the duct radius.

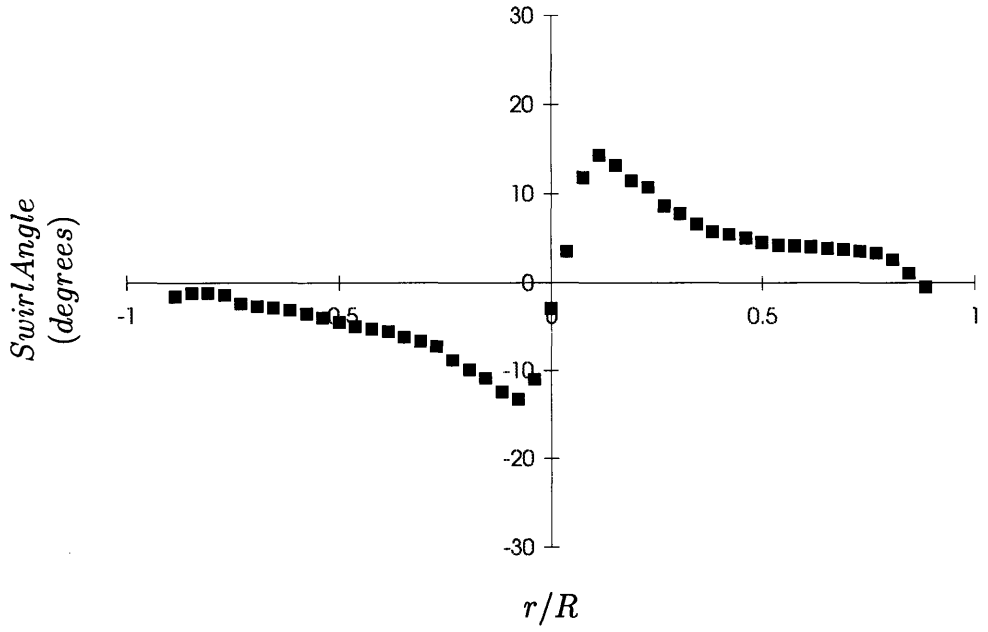

Figure A-1: Upstream Swirl Angle Profile for Vane Angle = 5 degrees

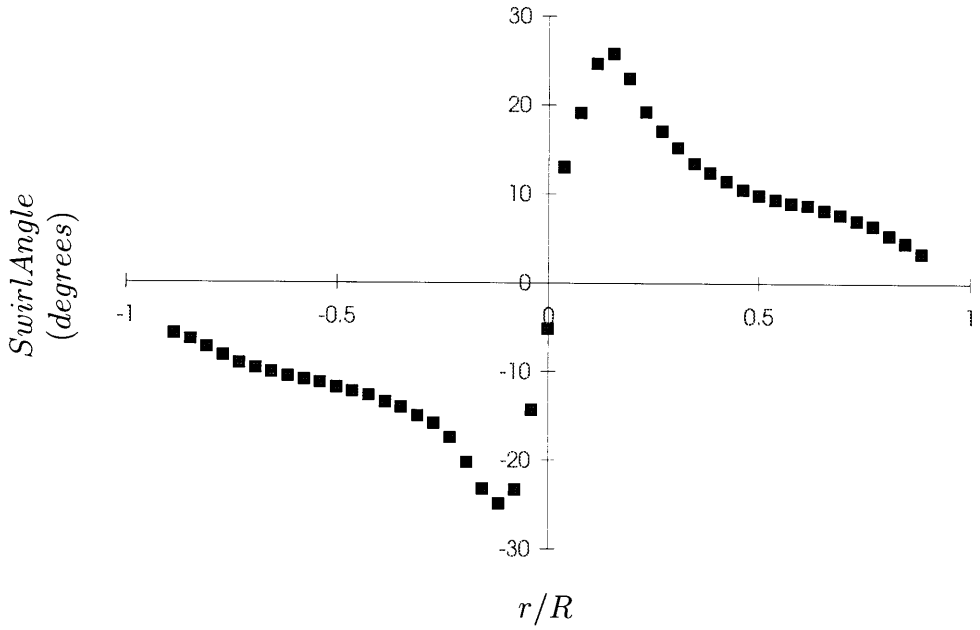

Figure A-2: Upstream Swirl Angle Profile for Vane Angle = 10 degrees

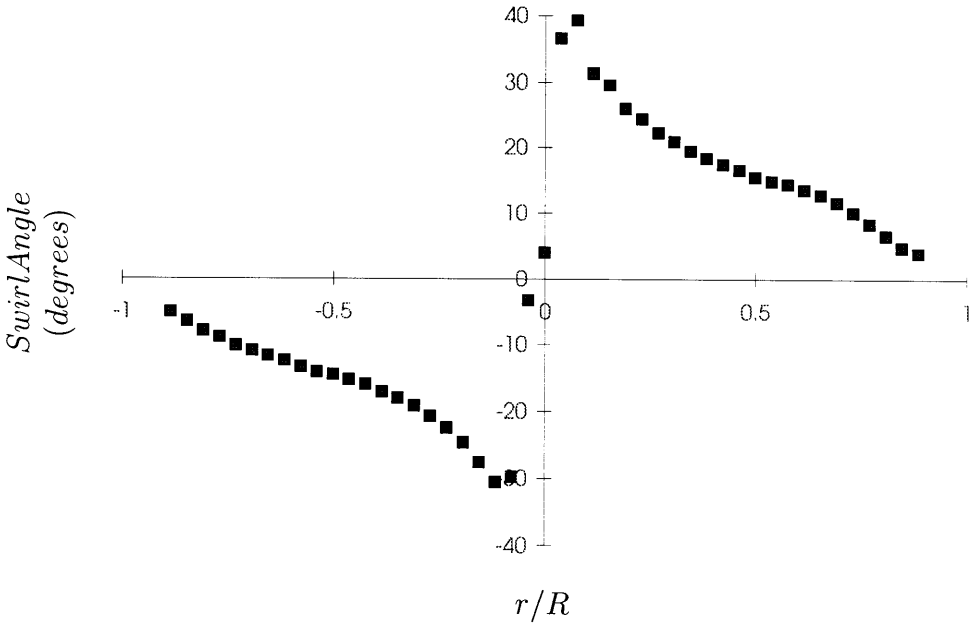

Figure A-3: Upstream Swirl Angle Profile for Vane Angle = 15 degrees

The following are samples of dynamic head profiles. Figures A-4, A-5, and A-6 are from the cases with vane angles set to 5, 10, and 15 degrees, respectively. The data was taken at the upstream station with no core injection. In these plots, Q is the local dynamic head, and P_{wall} is the static pressure measured at the wall at the same axial station.

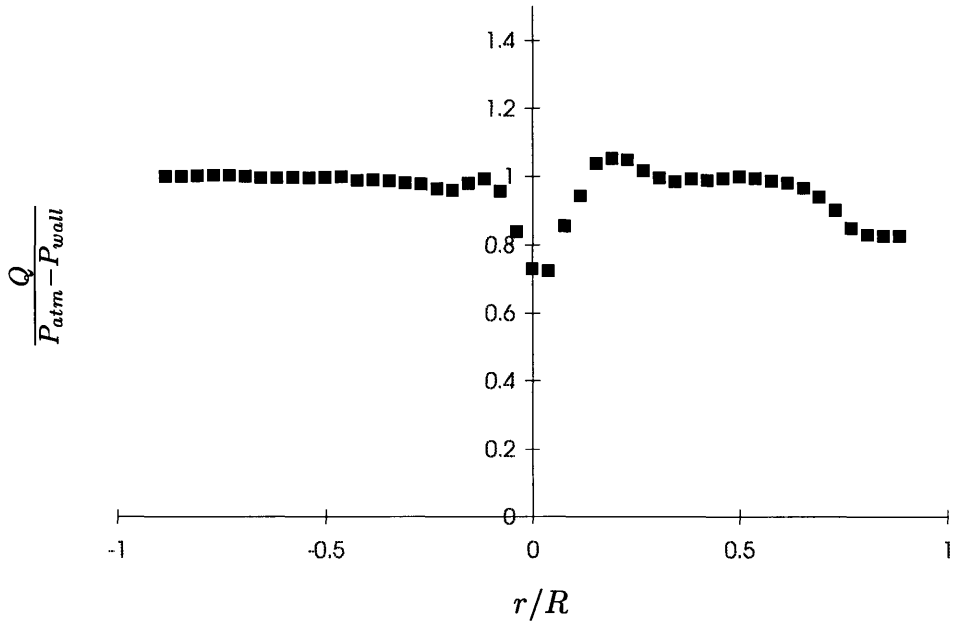

Figure A-4: Upstream Dynamic Head Profile for Vane Angle = 5 degrees

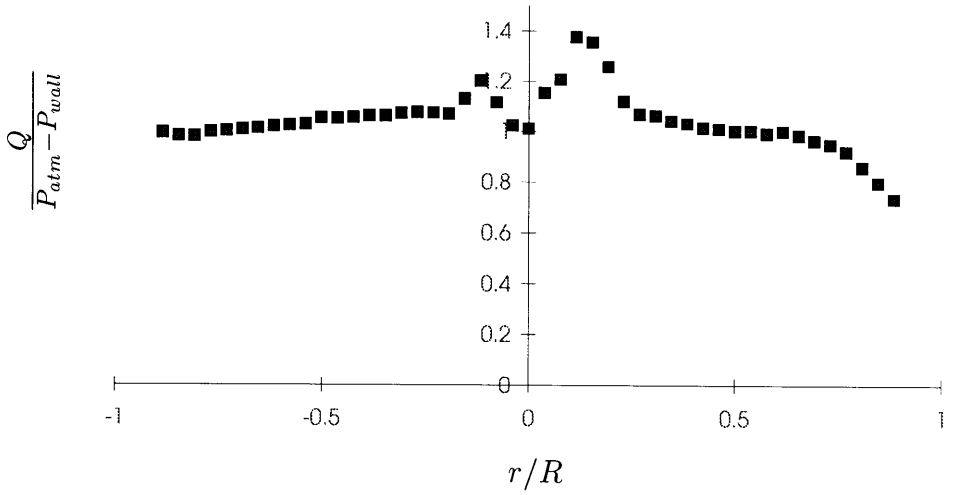

Figure A-5: Upstream Dynamic Head Profile for Vane Angle = 10 degrees

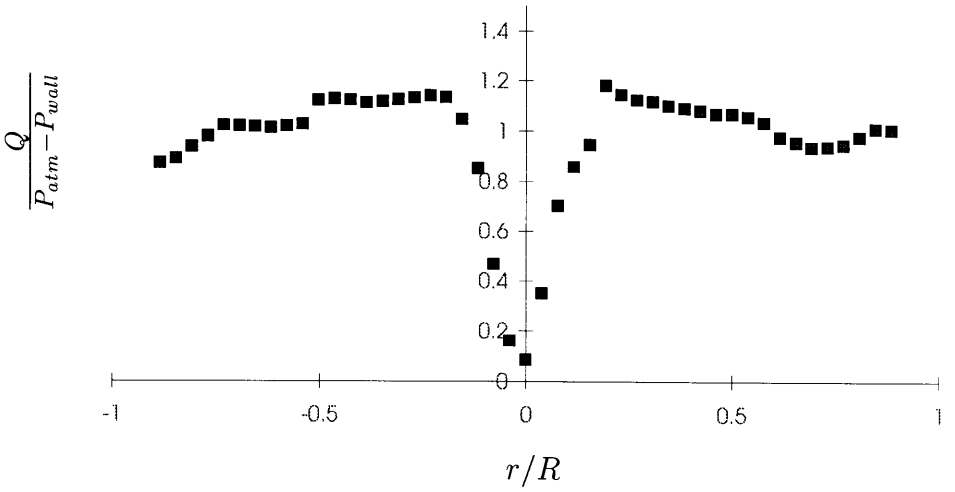

Figure A-6: Upstream Dynamic Head Profile for Vane Angle = 15 degrees

The following are samples of total pressure profiles. Figures A-7, A-8, and A-9 are from the cases with vane angles set to five degrees and with core injection levels of 0, 20, and 35 psi, respectively. The data was taken at the upstream station. In these plots, P_t is the local total pressure, P_{atm} is the atmospheric pressure, and Q_{fs} is the dynamic head of the free stream (outside the core).

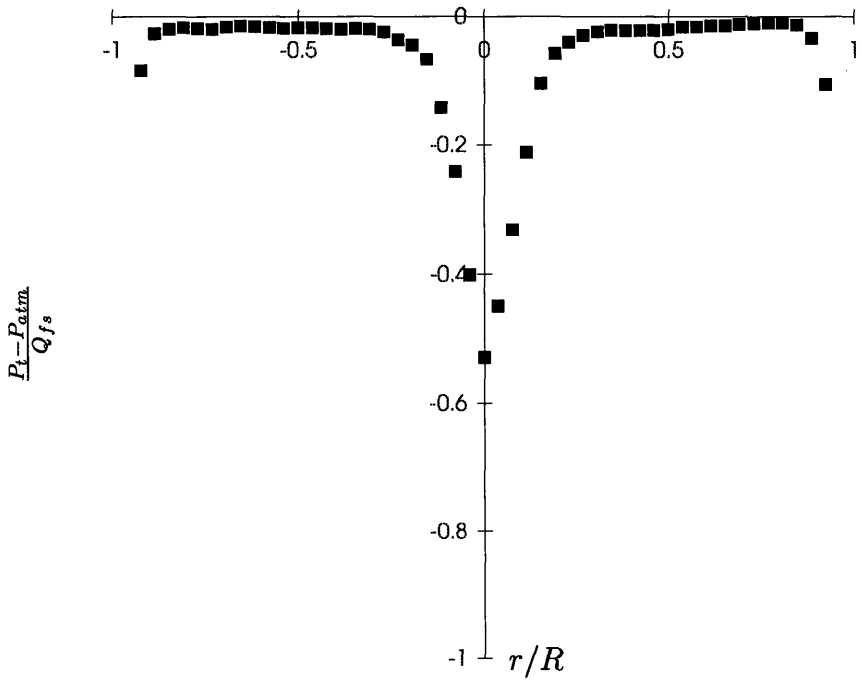

Figure A-7: Upstream Total Pressure Profile for Vane Angle = 5 degrees and Core Injection = 0 psi

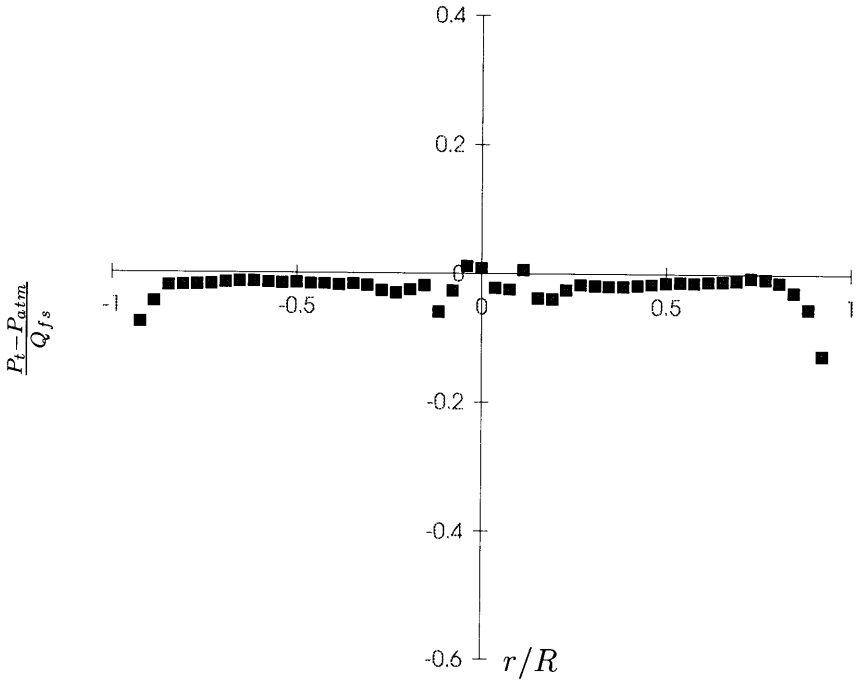

Figure A-8: Upstream Total Pressure Profile for Vane Angle = 5 degrees and Core Injection = 20 psi

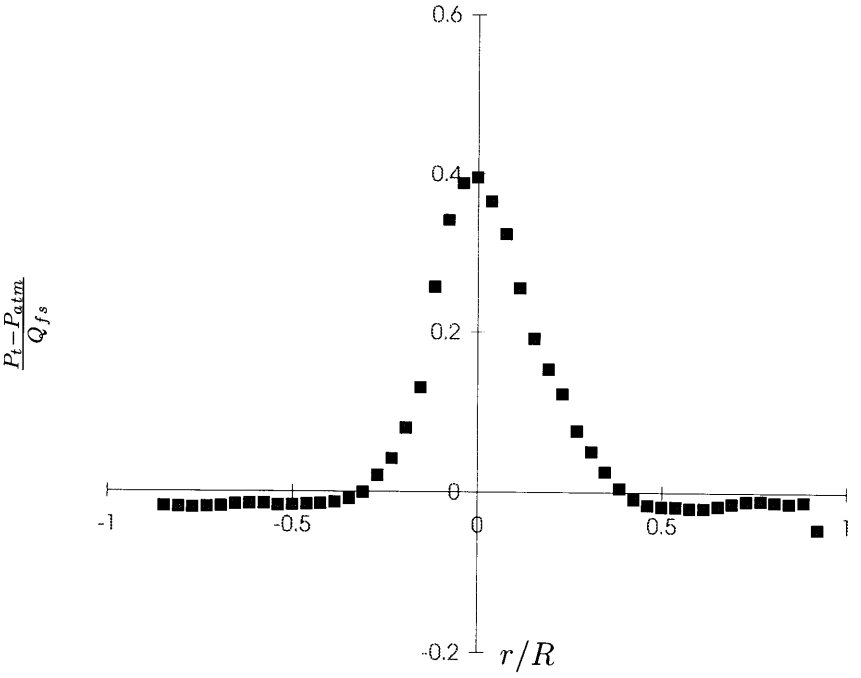

Figure A-9: Upstream Total Pressure Profile for Vane Angle = 5 degrees and Core Injection = 35 psi

A.2 Downstream Data

The following are samples of downstream swirl angle profiles. Figures A-10, A-11, and A-12 are from the cases with the static pressure rise set to 0, 50, and 75% of the inlet dynamic head, respectively, with the vane angles set to five degrees and with no core injection. In all figures, r is the local radius, and R is the duct radius.

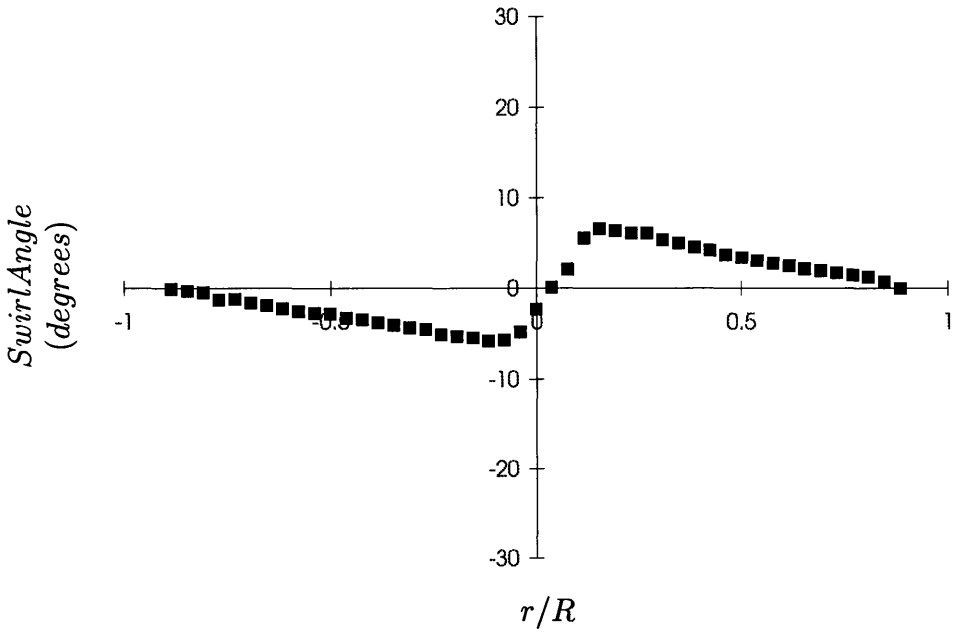

Figure A-10: Downstream Swirl Angle Profile for Vane Angle = 5 degrees and No Static Pressure Rise

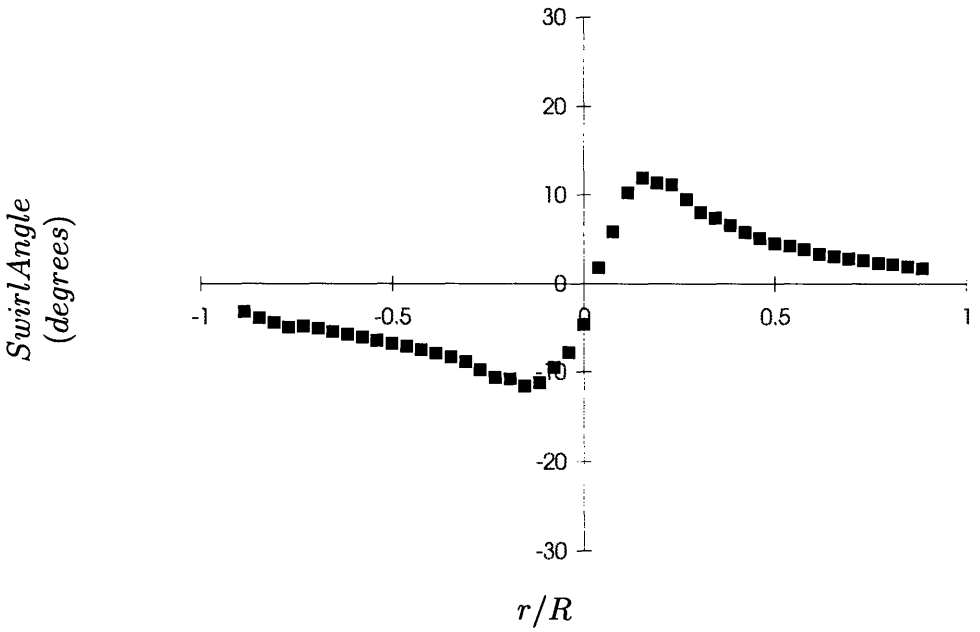

Figure A-11: Downstream Swirl Angle Profile for Vane Angle = 5 degrees and 50% Inlet Dynamic Head Static Pressure Rise

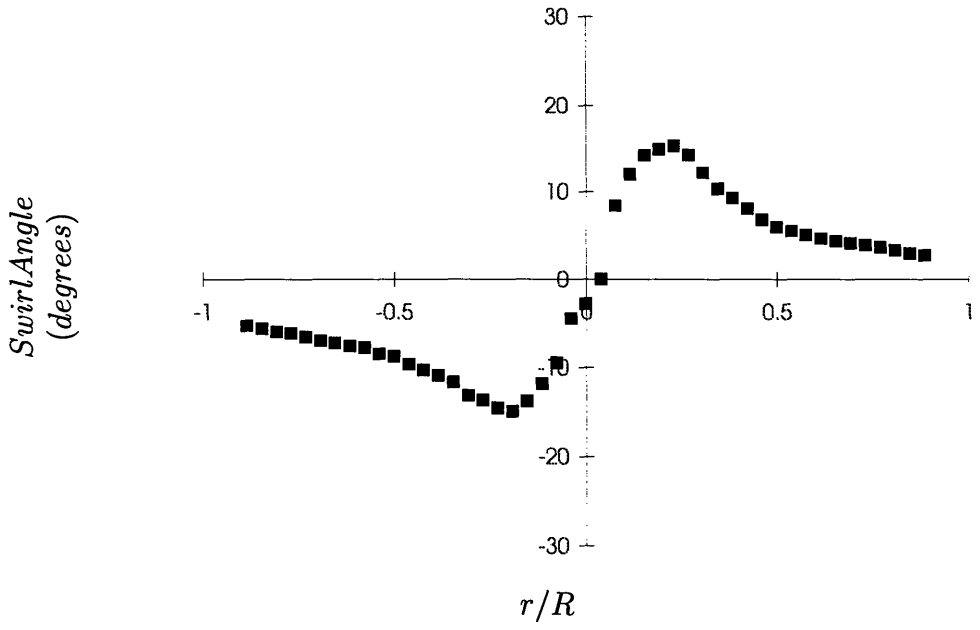

Figure A-12: Downstream Swirl Angle Profile for Vane Angle = 5 degrees and 75% Inlet Dynamic Head Static Pressure Rise

The following are samples of downstream dynamic head profiles. Figures A-13, A-14, and A-15 are from the cases with the pressure rise set to 0, 50, and 75% of the inlet dynamic head, respectively, with the vane angles set to five degrees and no core injection. In these plots, Q is the local dynamic head, and P_{wall} is the static pressure measured at the wall at the same axial station.

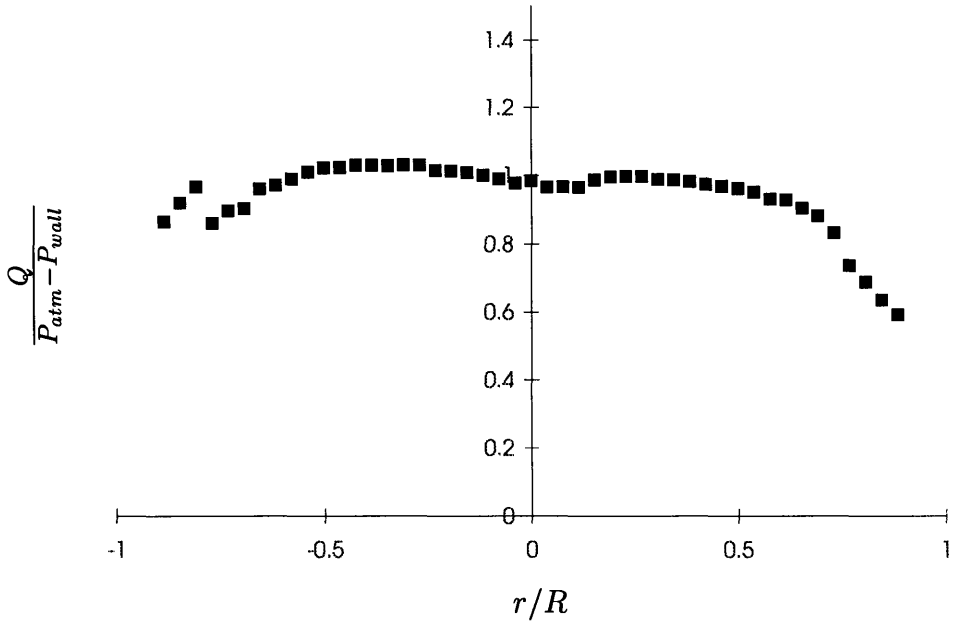

Figure A-13: Downstream Dynamic Head Profile for Vane Angle = 5 degrees and No Static Pressure Rise

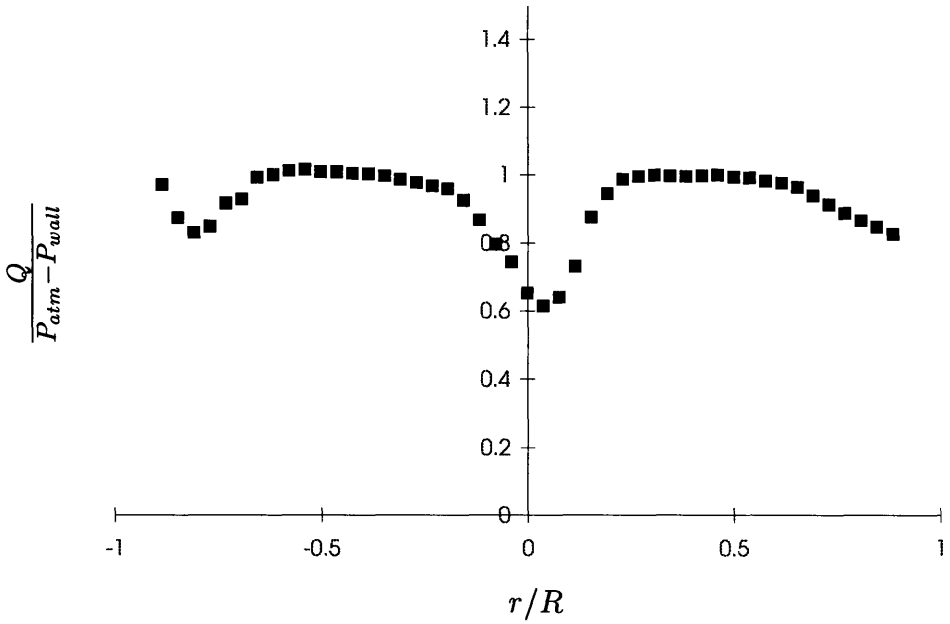

Figure A-14: Downstream Dynamic Head Profile for Vane Angle = 5 degrees and 50% Inlet Dynamic Head Static Pressure Rise

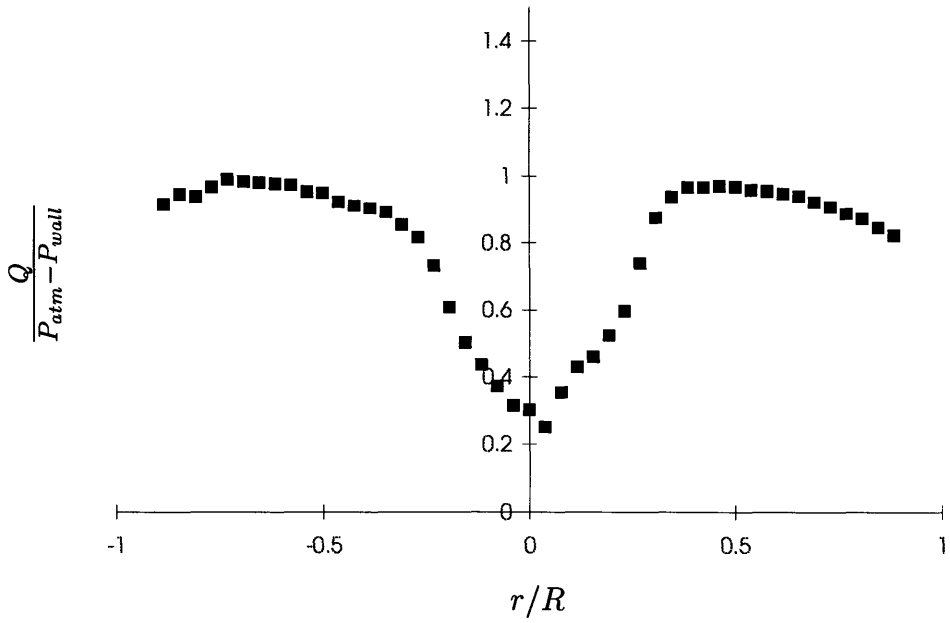

Figure A-15: Downstream Dynamic Head Profile for Vane Angle = 5 degrees and 75% Inlet Dynamic Head Static Pressure Rise

The following are samples of total pressure profiles. Figures A-16, A-17, and A-18 are from the cases with the static pressure rise set to 0, 50, and 75% of the inlet dynamic head, respectively, with the vane angles set to five degrees and with no core injection. In these plots, P_t is the local total pressure, P_{atm} is the atmospheric pressure, and Q_{fs} is the dynamic head of the free stream (outside the core).

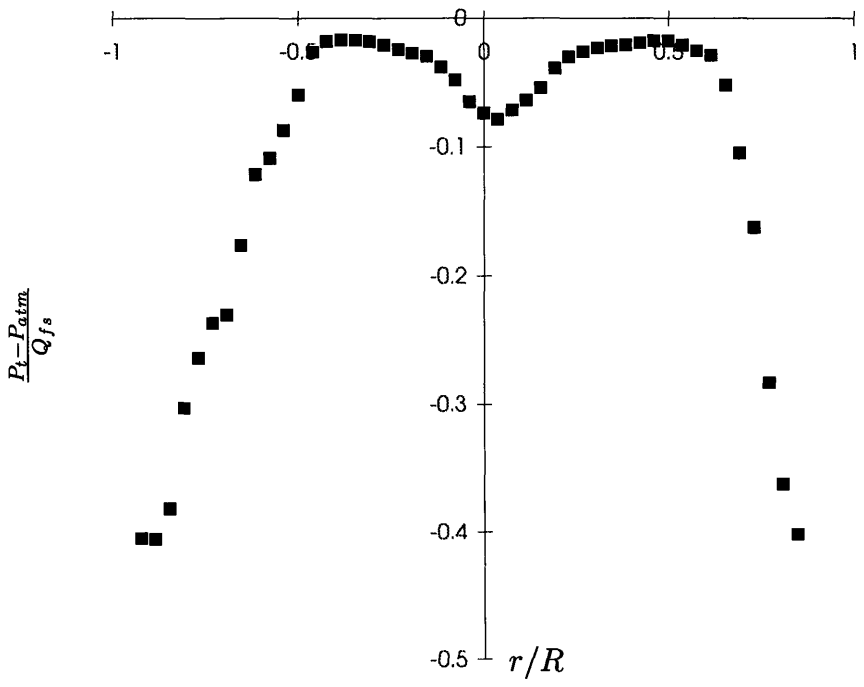

Figure A-16: Downstream Total Pressure Profile for Vane Angle = 5 degrees and No Static Pressure Rise

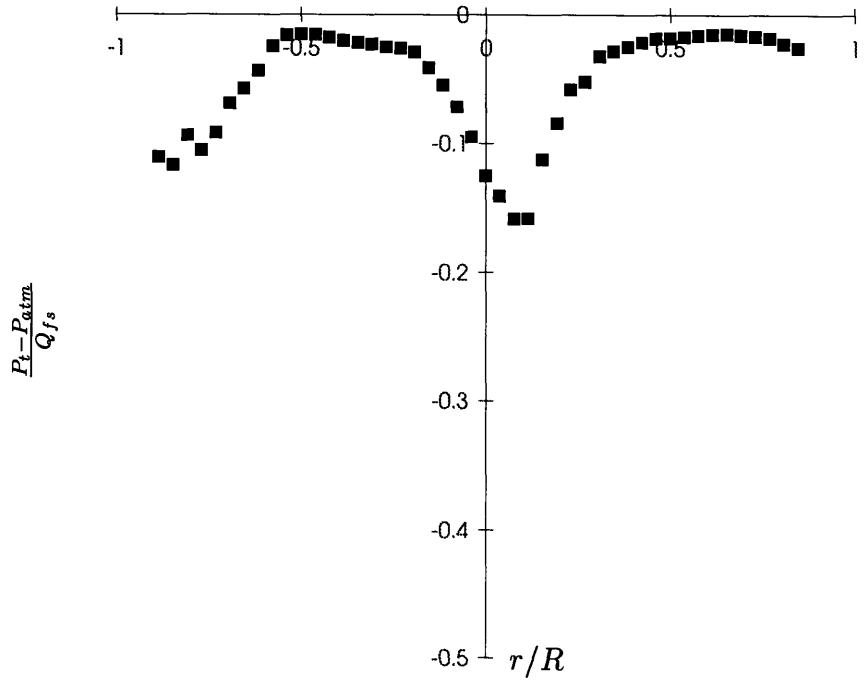

Figure A-17: Downstream Total Pressure Profile for Vane Angle = 5 degrees and 50% Inlet Dynamic Head Static Pressure Rise

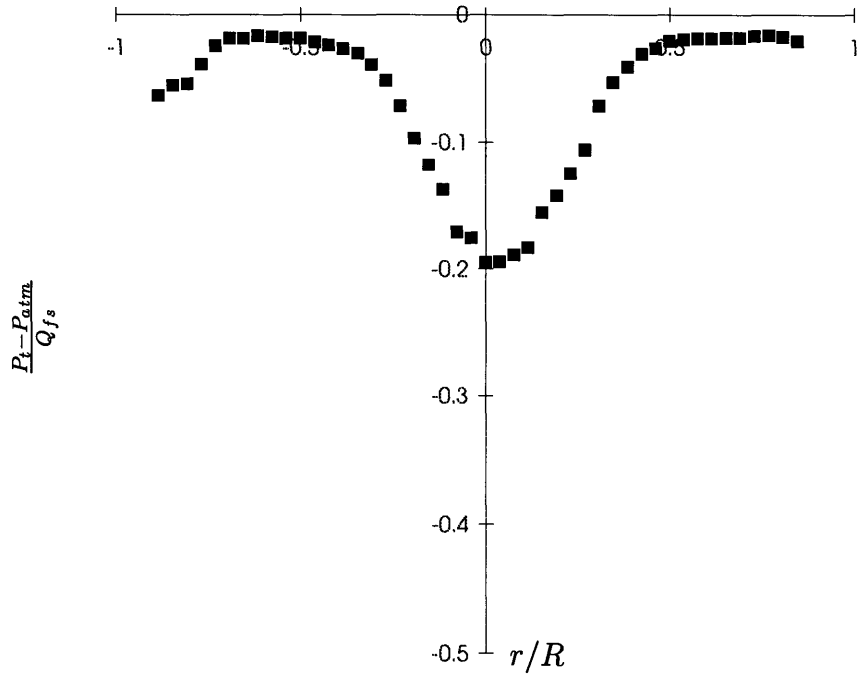

Figure A-18: Downstream Total Pressure Profile for Vane Angle = 5 degrees and 75% Inlet Dynamic Head Static Pressure Rise

Bibliography

[1] J. J. Adamczyk, M. L. Celestina, T. A. Beach, and M. Barnett. "Simulation of Three-Dimensional Viscous Flow within a Multistage Turbine," *ASME Journal of Turbomachinery*, Vol. 112, No. 3, pp. 370-376, 1989.

[2] J. M. Brookfield. "Vortical Flows in an Adverse Pressure Gradient," Master's thesis, Massachusetts Institute of Technology, June 1986.

[3] A. J. Crook. "Numerical Investigation of Endwall/Casing Treatment Flow Phenomena," Massachusetts Institute of Technology, August 1989.

[4] N. A. Cumpsty. Personal Communication, 1995.

[5] D. L. Darmofal. "A Quasi One-Dimensional Model for Axisymmetric Vortices in Pressure Gradients," Technical report, University of Michigan Department of Aerospace Engineering, August 1994.

[6] K. Hardie and A. Lengyel. "Vortex Bursting in Aircraft Engines," Massachusetts Institute of Technology, 16.622 Final Report, May 1993.

[7] P. G. Hill, U. W. Schaub, and Y. Senoo. "Turbulent Wakes in Pressure Gradients," *ASME Journal of Applied Mechanics*, December 1963.

[8] M. C. Johnson. "The Effects of Hub Treatment on Compressor Endwall Flowfields," Master's thesis, Massachusetts Institute of Technology, January 1985.

[9] S. A. Khalid. "The Effects of Tip Clearance on Axial Compressor Pressure Rise," PhD thesis, Massachusetts Institute of Technology, February 1995.

[10] A. S. Khalsa, 1993-95. Personal communication, PhD thesis not yet completed.

[11] R. Khan. "A Quasi One-Dimensional Analysis for Confined Vortex Cores," Master's thesis, Massachusetts Institute of Technology, February 1995.

[12] K. R. Kirtley, T. A. Beach, and J. J. Adamczyk. "Numerical Analysis of Secondary Flow in a Two-Stage Turbine," AIAA-90-2356, 1990.

[13] M. T. Landahl and S. E. Widnall. *Aircraft Wake Turbulence and Its Detection.* Plenum Press, 1971.

[14] N. K. W. Lee and E. M. Greitzer. "Effect of Endwall Suction and Blowing on Compressor Stability Enhancement," *Journal of Turbomachinery*, Vol. 112, January 1990.

[15] V. Modi. "A Theoretical Study of Flows in Compressor Hub/Casing Treatments," Internal M.I.T. Gas Turbine Laboratory Report, 1986.

[16] G. D. J. Smith and N. A. Cumpsty. "Flow Phenomena in Compressor Casing Treatment," *ASME Journal of Engineering for Gas Turbines and Power*, Vol. 106, No. 3, pp. 532=541, 1984.

[17] L. H. Smith. "Casing Boundary Layers in Multistage Axial-Flow Compressors," Flow Research on Blading, ed., L. S. Dzung, Elsevier, Amsterdam, 1970.

[18] K. L. Suder and M. L. Celestina. "Experimental and Computational Investigation of the Tip Clearance Flow in a Transonic Axial Compressor Rotor," ASME 94-GT-365, 1994.

[19] H. Takata and Y. Tsukuda. "Study on the Mechanism of Stall Margin Improvement of Casing Treatment," ASME Paper No. 75-GT-13, ASME Gas Turbine Conference, March 1975.

2556-24